DISS. ETH N° 21285

Measurements and evaluation of electron transport in electronegative gas mixtures

A dissertation submitted to

ETH ZURICH

for the degree of
Doctor of Sciences

presented by

Dominik A. Dahl

Master of Science in Physics
(Ernst-Moritz-Arndt-Universität Greifswald)
born on 20 January 1978
citizen of Germany

accepted on the recommendations of
Prof. Dr. Christian M. Franck
and Prof. Dr. Zoran L. Petrović

2013

Abstract

Within the framework of this thesis, a swarm parameter experiment (SParX) is designed, built, and operated. It implements the pulsed Townsend (PT) electrical method with a high degree of automatization. SParX is applied to investigate the electrical properties of gas mixtures containing strongly electronegative molecules, and the electron attachment parameters of selected molecules. Above all, the goal is to provide reliable and efficient techniques for characterizing and assessing gases considered as additives for gaseous insulation in high voltage applications.

A key component of SParX is the custom made pulsed electron source. It is built by a thin metal film photocathode in transmissive configuration, which is illuminated by short pulses of an ultraviolett laser system. Photocathodes of various metals have been produced, and they are investigated for their transmission spectra, photocurrent spectra, and quantum efficiencies. For the SParX setup, Palladium films are chosen as they perform most efficiently and stable in the presence of gases.

Intrinsic parameters of the measured PT swarm currents are identified. They comply with a temporal growth model of electron swarms. It is then possible, for the first time, to apply regression methods for obtaining the electron swarm parameters from PT measurements. These evaluation methods produce mutually independent parameters: Bulk drift velocity w, effective ionization rate constant ν_{eff}/N, and the gas density normalized diffusion time constant $N\tau_{\mathrm{D}}$.

The experimental setup and evaluation methods are tested with measurements in Ar, N_2 and CO_2, where the present results are found to satisfactorily match reference data. The operating regime of SParX is 1 to 11 kPa total gas pressure at 293 to 300 K, with

an electric field strength between 10 Td and 170 Td in N_2 (1 Td = 10^{-21} Vm^2 is the gas density normalized field strength E/N). SParX can provide high accuracy and (E/N)-resolution around $(E/N)_{\mathrm{crit}}$, where (ν_{eff}/N) is zero.

Measurements are made in binary mixtures with small amounts ($\leq$ 1.5%) of a strongly electronegative sample gas (SF_6 or C_3F_8) added to a buffer gas (Ar, N_2 or CO_2). A linear relation between the mixing ratio and ν_{eff}/N is apparent, and it is feasible to evaluate the sensitivity of ν_{eff}/N to changes of the mixing ratio. This analysis technique produces the linear response parameters as a function of E/N. These parameters characterize gas mixtures by representing the influence of the electron energy distribution of a buffer gas on the electron attachment rates of a sample gas.

The PT method and the linear response technique are applied to investigate octafluorotetrahydrofuran (c-C_4F_8O), a gas with previously unknown swarm parameter values. The measurements provide swarm parameters and $(E/N)_{\mathrm{crit}}$ for mixing ratios of c-C_4F_8O $\leq$ 1.2% in buffer gases. It is feasible to estimate preliminary electron attachment cross sections of c-C_4F_8O, which are consistent with the presently measured attachment parameters.

Two criteria are used to assess the electrical performance of gas mixtures: The linear response parameters as a function of E/N, and $(E/N)_{\mathrm{crit}}$ as a function of the mixing ratio. For all the sample gases tested, their mixtures with N_2 can provide higher $(E/N)_{\mathrm{crit}}$ than the mixtures with CO_2. It is found that $(E/N)_{\mathrm{crit}}$ of N_2/c-C_4F_8O reaches 85% of the benchmark N_2/SF_6 for small mixing ratios. High attachment rates can appear in N_2/c-C_4F_8O because the attachment cross sections of c-C_4F_8O overlap with densely populated intervals of the electron energy distribution in N_2. However, in this mixture we see indications of delayed electron production with concurrent dissociation processes for $(E/N) > (E/N)_{\mathrm{crit}}$.

Kurzfassung

Im übergeordneten Rahmen einer Beurteilung von SF_6-Substituten wird in dieser Arbeit ein Schwarm Parameter Experiment (SParX) aufgebaut. Eine gepulste Townsend (PT) Methode wird eingesetzt, wobei ein Schwarm freier Elektronen erzeugt und dessen Verschiebestrom in Gas gemessen wird. In SParX bestimmen wir die elektrischen Eigenschaften von Gasmischungen mit mindestens einer elektronegativen Komponente und untersuchen die Elektronenanlagerung an Moleküle. Das Hauptziel ist die Bereitstellung von zuverlässigen und effizienten Methoden zur Bewertung von Mischungskomponenten einer Gasisolation für die Hochspannungstechnologie.

Ein Schlüsselelement von SParX ist die selbst entwickelte gepulste Elektronenquelle. Diese besteht aus einer transmissiven Metallfilm-Photokathode, die rückseitig von einem Ultraviolett-Laser mit kurzen Pulsen beleuchtet wird. Photokathoden aus verschiedenen Metallen wurden produziert und charakterisiert mittels Transmissions-Spektrum, Photostrom-Spektrum und ihrer Quanteneffizienz. Schliesslich setzen wir Palladium-Filme in SParX ein, die in Gasen sehr effizient und zuverlässig arbeiten.

PT Stromkurven repräsentieren die Entwicklung eines Elektronenschwarms in der Zeit. Die intrinsischen zeitlichen Parameter zur Beschreibung der Stromkurven werden identifiziert. Somit ist es erstmals möglich, die Stromkurven in Regressionsanalysen auszuwerten, bei denen die Gasdichte und der Elektrodenabstand als unabhängige Parameter eingehen. Diese sehr sensitiven Analysemethoden ergeben drei wechselseitig unabhängige Parameter von Elektronenschwärmen: Driftgeschwindigkeit w des Schwarms, effektive Ionisationsratenkonstante ν_{eff}/N, und die auf Gasdichte normierte Zeitkonstante $N\tau_{\text{D}}$ der Elektronendiffusion.

Der Experimentaufbau und die Auswerteverfahren werden getestet mit Messungen in Ar, N_2 und CO_2, die gut mit Referenzdaten übereinstimmen. Der Betriebsbereich von SParX ist 1 bis 11 kPa Gasdruck bei 293 bis 300 K, elektrische Feldstärken zwischen 10 Td und 170 Td in N_2 (1 Td = 10^{-21} Vm^2 ist die auf Gasdichte normierte Feldstärke E/N). SParX verfügt über eine hohe (E/N)-Auflösung und Genauigkeit im Bereich um $(E/N)_{\text{crit}}$, wo ν_{eff}/N null ist.

Messreihen in binären Mischungen werden durchgeführt, wobei kleine Anteile ($\leq 1.5\%$) eines stark anlagernden Gases (SF_6 oder C_3F_8) einem Hintergrundgas (Ar, N_2 oder CO_2) beigemischt werden. Man fand eine lineare Relation zwischen dem Mischungsverhältnis und ν_{eff}/N. Mit dieser Relation bestimmen wir die Sensitivität von ν_{eff}/N auf eine Änderung im Mischungsverhältnis. Diese Auswertungstechnik ergibt lineare Antwortparameter als Funktion von E/N, welche charakteristisch für Gasmischungen sind. Sie beschreiben den Einfluss der Elektronenenergie Verteilung des Hintergrundgases auf die Elektronen Anlagerungsrate des Probengases.

Wir untersuchen Octafluorotetrahydrofuran (c-C_4F_8O) in SParX. Kleine Anteile $\leq 1.2\%$ von c-C_4F_8O werden Hintergrundgasen beigemischt, und erstmalig werden $(E/N)_{\text{crit}}$ und die Schwarmparameter gemessen. Eine Sensitivitatsanalyse wird durchgeführt, und aus den linearen Antworten werden Anlagerungsquerschnitte von c-C_4F_8O vorhergesagt, die mit den Messungen konsistent sind.

Zur Bewertung der elektrischen Festigkeit von Gasmischungen wenden wir zwei Kriterien an: Die lineare Antwort als Funktion von E/N, und $(E/N)_{\text{crit}}$ als Funktion des Mischungsverhältnisses. Die hier untersuchten Probengase ergeben höhere $(E/N)_{\text{crit}}$ in N_2 als in CO_2. Bei N_2/c-C_4F_8O erreicht $(E/N)_{\text{crit}}$ 85% des Wertes von N_2/SF_6. Die Raten der Elektronenanlagerung in N_2/c-C_4F_8O sind relativ hoch, weil die Anlagerungsquerschnitte von c-C_4F_8O sehr günstig sind für die Elektronen Energieverteilung in N_2. Es gibt aber Hinweise auf mögliche Schwachpunkte dieser Mischung: Verzögerte Elektronenproduktion und Dissoziation von c-C_4F_8O werden beobachtet bei $(E/N) > (E/N)_{\text{crit}}$.

Contents

1. Introduction

Gas mixtures described as *electronegative* comprise at least one component capable of forming negative ions of relatively long lifetime (≥ 1 ns). The atmosphere of the earth is such an electronegative gas mixture [1]. Electron attaching gases are technologically important as they support key processes such as:

- Etching and cleaning in semiconductor manufacture [2, 3].
- Enhanced lean combustion [4].
- Gas based radiation detectors [5, 6].
- Electron scavenging in high voltage gas insulation [7, 8].
- Arc quenching in high current switching [9].

The underlying processes can be fairly well understood and modelled on the basis of the kinetic theory of gases [10]. It describes electrical and chemical processes in gases and gas mixtures. A strong knowledge base has been established with the kinetic theory at the core. For the applied research in a particular domain, it seems to be advisable and beneficial to maintain strong connections to the general kinetic theory.

The present investigation is concerned with the electron kinetics of electronegative gas mixtures. The analysis is focused on the aspect of gas insulation in high voltage technology. Gas mixtures, which consist of one or two attaching gases and one or two buffer gases, are of particular interest because they are considered as a prospective replacement for pure SF_6 [7, 11]. An objective of the present work is to provide methods and fundamental data for efficiently assessing the electrical properties of such gas mixtures.

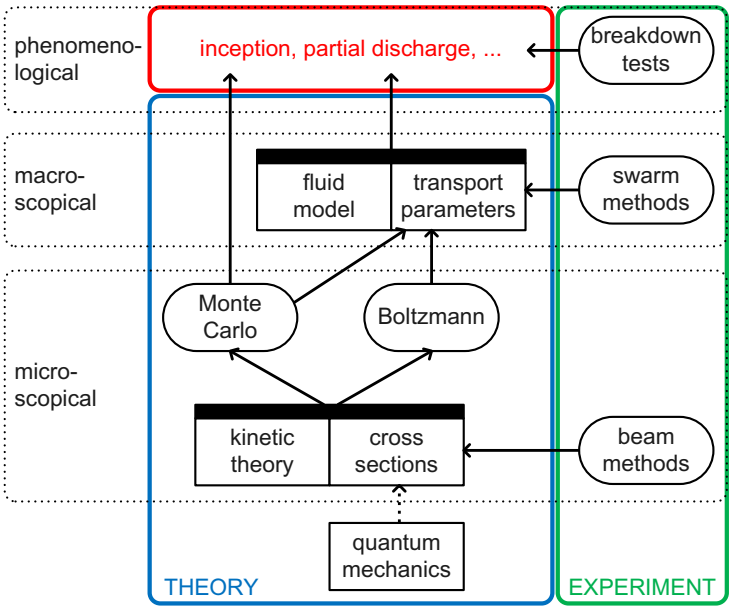

Figure 1.1.: Scheme of selected theoretical and experimental methods for investigating electrical phenomena in gases.

1.1. Methodology for studies of gas discharges

Electrical phenomena in gases play an important role in high voltage technology. For instance, one has to deal with

- determining the electrical conductivity of gases.
- the inception of a gas discharge.
- the occurence of partial streamer discharges.
- gas breakdown of technical equipment.

These phenomena can be reproduced in laboratory experiments [11], which will, however, provide only minor insight in the macroscopical and microscopical processes involved with a particular phenomenon. On the other hand, these phenomena can be represented

by physical models, which require the input of accurate fundamental data on all relevant processes.

1.1.1. Microscopical approaches

On a microscopical level, the phenomena are fully described by kinetic theory. However, it turns out that the associated equations can only be solved exactly in particular cases [10]. The equations can be treated analytically to allow for sufficiently accurate numerical solutions in some practically relevant cases [12]. In order to obtain solutions for the general problem, one can attempt to simulate the evolution of a physical system under the laws of kinetic theory, using Monte Carlo methods for example [5, 13]. It should then be possible to compute the evolution of a discharge using a microscopical approach, however, it is still a formidable, resource-intensive and time-consuming task.

The input data consist of a set of cross sections representing the interaction of electrons with the gas particles. Such cross sections can be measured using beam methods [14]. In particular cases, the cross sections can be determined ab intio [15]. However, it turns out that beam methods and quantum mechanics are generally not sufficient to produce a set of cross sections consistent with a particular phenomenon [16].

1.1.2. Macroscopical approaches

One can simplify the rigorous kinetical description of the system by making assumptions [17], in order to obtain a set of equations which can be solved using analytical or numerical methods. This approach leads to a macroscopical fluid model of the phenomenon under study. Fluid models require the input of a set of transport parameters [17]. Discharges in technical equipment can be sufficiently described with the knowledge of a complete set of transport parameters. Those include for example the transport parameters of

1. electrons and ions,

2. momentum,

3. and energy.

These transport parameters depend on E/N, which denotes the electric field strength per gas particle, given in units of Townsend ($1\ \mathrm{Td} = 10^{-21}\ \mathrm{Vm}^2$). Transport parameters can be measured, as it is done for example in the present work. Alternatively, they can be determined from the underlying kinetic theory if complete sets of the relevant cross sections are known, using Monte Carlo methods or a solution of the Boltzmann equation [5, 12, 18, 19].

1.1.3. Experimental electron swarm methods

Measurements of the macroscopical electron swarm parameters play a very central role in studies on electrical phenomena in gases. The swarm results can be identified with the electron transport parameters [10, 20]. Under ideal swarm conditions, it is not necessary to treat momentum and energy transport separately from particle transport. It is a widely accepted best practice to test fluid models and microscopical methods for their ability to reproduce the evolution of electron swarms [17].

There is a distinction between three classical types of swarm experiments [19]:

- Time-of-flight (TOF) methods produce the electron drift velocity w and electron diffusion coefficients.

- Steady-state Townsend (SST) methods produce spatial ionization coefficients α_{eff}/N.

- Pulsed Townsend (PT) methods comply with a temporal swarm model, and they can produce drift/diffusion and ionization data at the same time.

In order to obtain a complete set of swarm parameters, it was necessary to combine results from TOF and SST, i.e. from different

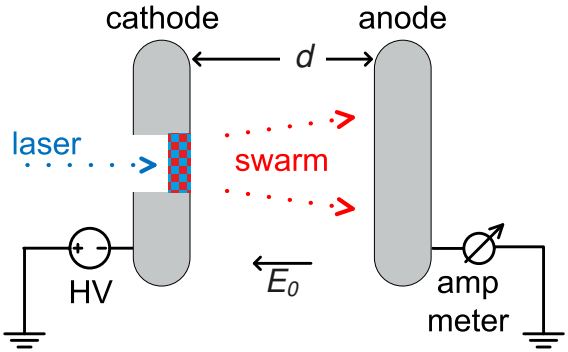

Figure 1.2.: Illustration of the projected pulsed Townsend setup. Two electrodes at spacing d provide a homogeneous electric field E_0. A high voltage (HV) is applied to the cathode, and the anode is connected to an ampere meter. The arrows (·····>) indicate the laser illumination of a photocathode, and the drift of an electron swarm.

experiments based on different swarm models. The merged set can be inconsistent because α_{eff}/N depends on w. An advantage of PT is the capability to provide a complete, consistent set of swarm parameters.

PT methods were successfully used many times in the past, and they are an integral part of the methodology of modern plasma physics and molecular physics [20].

1.2. Choices of methods

An intention of the present work is to setup a PT experiment [21], and to apply the PT method for investigating gas mixtures containing strongly electronegative gases. It is anticipated that a PT experiment can efficiently produce the necessary results for assessing the electrical properties of gas mixtures suitable for high voltage insulation applications [22].

Figure 1.2 is a schematic representation of the projected PT ex-

periment. Basically, it consists of two electrodes inside a vacuum chamber which is filled with a gas sample. By a short laser pulse, an ensemble of photoelectrons is generated at the cathode. It drifts through the sample gas at constant average velocity in a homogeneous electric field. The collective motion of these electrons under the influence of their interactions with the gas particles is modelled as a swarm. The swarm motion gives rise to a displacement current which is recorded and analysed.

In order to benchmark the present methods, one can consult reference data from previous swarm measurements. In addition to experimental swarm data, it is desired to access supplementary or complementary data which have been based on beam methods or quantum mechanics. Standard numerical techniques are applied for simulating or calculating electron transport parameters with the input of cross sections taken from the literature. We use a Monte Carlo swarm method (Magboltz [5]), and a solver (Bolsig+ [18]) for the Boltzmann equation.

1.3. Project outline

It is attempted to successively approach the project goal with the following steps:

1. Implementing a pulsed electron source. This key component of the experimental setup shall be described in chapter 2.

2. Setting up the PT experiment. It is presented in chapter 3, together with the measurement procedures.

3. Developing a temporal growth model of electron swarms in gases to serve as the basis for signal processing. This model is defined in chapter 3.

4. Performing benchmark measurements in gases with well known swarm parameters. The benchmark results are presented in chapter 3.

5. A technique for investigating gas mixtures that contain strongly electronegative gases, the so-called linear response technique, shall be developed in chapter 4.

6. The proof of principle of the linear response technique is made in chapter 4.

7. In chapter 5 the present set of methods is applied to investigate c-C_4F_8O, a gas with hitherto unknown swarm parameters.

Every individual chapter terminates with a conclusions section. General conclusions of the present work are given in chapter 6.

2. Pulsed electron source

Parts of this chapter have been published [22].

2.1. Introduction

In the present context, a pulsed electron source (PES) consists of a photocathode and a pulsed laser system. Photocathodes are widely used in vacuum [23–25]. In contrast, in PT experiments [26–29] and in radiation detectors with gas amplification [30], the photocathode necessarily operates in the presence of gases, i.e. ∼100 Pa to ∼100 kPa total pressure. Under these conditions, one must consider the adsorption of gas molecules on the photocathode surface [31], and the non-equilibrium interaction of photoelectrons with the gas particles in the immediate vicinity of the cathode [30].

A photocathode for PT applications is required to meet the following conditions:

1. It should withstand the impact of ions and radicals, which are generated from the sample gases in the PT discharge.

2. It must not disturb the homogeneous electric field within the PT setup.

3. It should be conductive with a low-ohmic, high-bandwidth electrical bonding.

4. A large active area of the photocathode is desired.

This chapter describes the design and the manufacturing process of an efficient, resistant photocathode which can be conveniently

used in a PT setup. We investigate the characteristics of the photocathode and the performance of the PES in the presence of gases.

For the reader's convenience, a conversion factor is given between the photon energy ε_p and the photon wavelength λ.

$$\varepsilon_\mathrm{p}\lambda = 1240\ \mathrm{eV\,nm} \tag{2.1}$$

2.1.1. Photocathodes in ultra-high vacuum

Photocathodes are characterized by their electric work function Φ, which is the photon energy ε_p required to release an electron into vacuum at 0 K and with the electric field extrapolated to zero [32]. The quantum efficiency (QE) of a photocathode is the number of electrons n_e per incident photons n_p.

$$\mathrm{QE} = \frac{n_\mathrm{e}}{n_\mathrm{p}}\ . \tag{2.2}$$

For $\varepsilon_\mathrm{p} \approx \Phi$, the QE strongly varies with small changes of ε_p, as it is described by Fowler's theory [32].

We are particularly interested in thin film photocathodes because thin films can have a lower Φ than the corresponding bulk material [23]. A theory of the QE of thin film photocathodes was described previously [23].

The PES can be realized in two geometrical configurations:

- A reflective photocathode: Photoelectrons are emitted from the illuminated face.
- A back-illuminated transmissive photocathode [33]: Photons impact on one face and photoelectrons emerge from the opposite face.

Gold film (Au) photocathodes are widely used for PES in vacuum. There are recent implementations of an Au film in a transmissive configuration [23,24], as well as in a reflective configuration [25]. In these experiments, special precautions are required to obtain stable

and reproducible values of Φ and QE [31, 34]. Usually the photocathode is maintained in ultra-high vacuum after a bake-out of the vacuum system.

2.1.2. Photocathodes for PT

A well established PES for the PT application comprises a bulk metal photocathode. In many cases a stainless steel cathode was used in conjunction with a 266 nm laser system [26, 27, 35]. In other cases an aluminum cathode was used with a 355 nm laser [28] or a 337 nm laser [29]. In these cases the laser pulse energy used to be between 120 μJ and 20 mJ.

There are previous reports on successful implementations of a PES with a thin film photocathode in a transmissive configuration. The following film materials have been used, amongst others:

- Gold (Au) [36, 37].
- Aluminum (Al) [38].
- Palladium (Pd) [39].

The QE of a PES can be strongly influenced by the interaction between gas species and the cathode surface. In the case of an Al cathode, oxygen adsorption can cause a decrease of Φ, and consequently, Φ increases when the adsorbed oxygen is removed due to the PT discharge [38]. In the case of an Au cathode, the QE of the PES collapses in a discharge containing nitrogen (see 2.3.4).

2.1.3. Surface effects of palladium films

A clean Pd surface is not thermodynamically stable at room temperature, 300 K, in vacuum, 10^{-5} Pa [31]. The residual gas molecules interact with the Pd film in many ways, for example:

- Pd absorbs hydrogen (H), and the equilibrium H concentration is reached within less than one second [40].

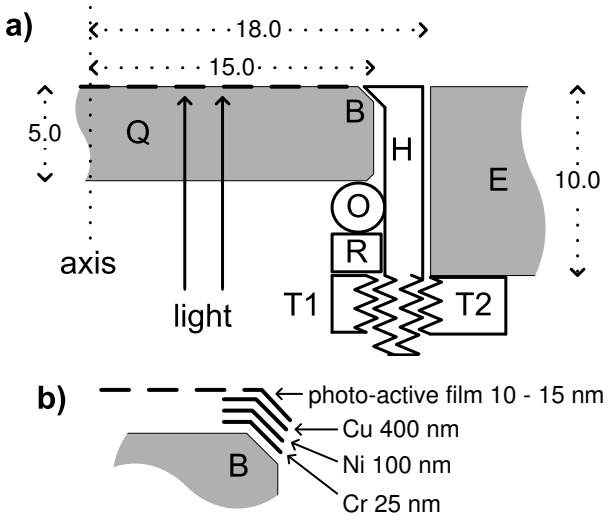

Figure 2.1.: (a) Axially symmetric drawing of the photocathode and the photocathode mount. The photo-active layer (– – –) is back-illuminated as indicated by solid arrows. Dimensions (· · · · · ·) are given in mm. See section 2.2.1 for a comprehensive description. Panel (b) is a schematic of the coating layers at the bevel B.

- H can be split from hydrocarbons at the Pd surface [34].
- A layer of adsorbed oxygen can cause an increase of Φ by e.g. 0.43 eV [40].
- Oxygen reacts with H to form OH [34].

2.2. Experimental methods

2.2.1. Photocathode and its mount

We use z-cut, polished quartz windows as the photocathode substrates. Figure 2.1 shows the dimensions and the geometry of the

substrates. One bevel (label B in figure 2.1) of the quartz Q was cut 45° 1.3 mm wide. The coatings were applied by electron beam evaporation. Using a microbalance, the film thickness was controlled with a precision of ±1 nm. The bevel B was coated with robust contact layers, as indicated in figure 2.1(b). In the final step, the whole face of the quartz was coated by a photo-active film which has an active area of 25 mm diameter.

The photocathode is mounted as shown in figure 2.1(a). The coated quartz Q is fixed in the holder H by a viton o-ring O which is pressed by the thread ring T1. While being screwed, T1 can slide at the interface with a metal ring R, thus a twisting of O is avoided. An electrical contact is established between B and H. Another thread ring T2 is fixed to the electrode E. The holder H is screwed into T2 such that the photocathode surface and H are adjusted to the level of the electrode surface. The residual level difference is less than 0.2 mm.

2.2.2. Optical components

Lamps

A 200 W mercury arc quartz lamp (HBO), and a 150 W xenon arc spectrosil lamp (XBO) have been used. The collimated light of these lamps was directed through a monochromator of focal length 250 mm with a 1200 grooves/mm grating. Using the Hg emission lines, the wavelength axis of the monochromator was calibrated with a precision ±1 nm. The dimensions of the entrance and exit slits of the monochromator were set to produce a Gaussian instrumental broadening of 5 nm FWHM.

Laser system

A passively Q-switched Nd:YAG laser (CryLas FQSS-266) was used to generate pulses with 266 nm wavelength. The pulse duration was 1.5 ns FWHM, and the repetition rate was 20 Hz. The pulse energy

exhibited a fluctuation of $\approx 1\%$ standard deviation. We determined an absolute pulse energy (152 ± 5) µJ at the sample.

Photodetectors

- A caloriemeter was used to measure the absolute spectral intensity of the HBO.
- A calibrated pyrodetector served for measuring the laser pulse energy.
- This pyrodetector, in combination with a mechanical chopper, served for recording the relative spectral intensity of the XBO.
- A photomultiplier (Hamamatsu H10720-110) served for determining the temporal profile of the laser pulse.

2.2.3. Electrode setup

DC setup

As it is represented in figure 2.2, two plane aluminum electrodes with spacing $d = 2$ mm are installed in a bell-jar vacuum chamber ($< 10^{-5}$ Pa). The anode is set to a potential $U = 14$ V, and the cathode is connected to a picoampere meter. The photocathode is mounted in a transmissive configuration. Through a quartz window, it is illuminated by monochromatic light (see section 2.2.2). The illuminated area on the sample covered approximately 18×12 mm^2.

Pulsed Townsend setup

Figure 2.3 shows a schematic diagram of the PT setup. The electrodes are installed in a vacuum chamber ($< 10^{-5}$ Pa) where we can chose to fill in a sample gas. The electrode spacing d can be set between 2 and 27 mm. The cathode is connected to a DC high voltage source, and the anode is connected to a transimpedance amplifier (FEMTO DHPCA-100) with variable gain. The low voltage

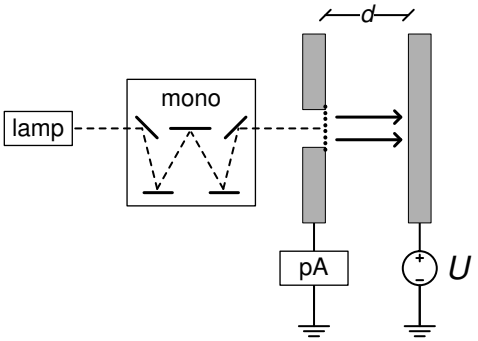

Figure 2.2.: Optical arrangement and electric circuit diagram for measuring photocurrent spectra. The two electrodes with spacing d are within a vacuum chamber. The anode is connected to a voltage source U, the cathode is connected to a picoampere meter (pA). The light (– – –) of the lamps passes a monochromator and illuminates the photocathode (· · · · · ·). Arrows indicate the motion of the photoeletrons.

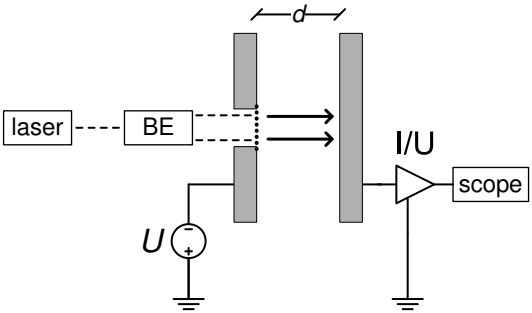

Figure 2.3.: Optical arrangement and electric circuit diagram of the PT setup. The two electrodes with spacing d are within a vacuum chamber. The laser beam (– – –) illuminates the photocathode (· · · · · ·) via a beam expander (BE). Arrows indicate the swarm drift direction. The cathode is connected to a voltage source U. The anode is connected to the oscilloscope via a transimpedance amplifier (I/U).

circuit was optimised to provide a high signal bandwidth (200 MHz) and high fidelity. The laser beam (see section 2.2.2) is expanded to cover the whole active area, 25 mm diameter, of the photocathode. A photodiode is used to trigger an oscilloscope for recording the current waveforms of photoelectrons or electron swarms.

2.2.4. Determination of quantum efficiency

The QE is calculated using (2.2). A measurement of the wavelength and intensity of the illumination yields n_p. In the case of a DC photocurrent, n_e can be measured directly. In the case of photocurrent pulses, the electron number n_e can be determined using the following equations.

Photocurrent pulse in vacuum

In vacuum the photocurrent $I_{\mathrm{PT}}(t)$ is generated by electrons which are steadily accelerated in the applied homogeneous electric field. According to classical mechanics, n_e can be estimated from the peak value $\hat{I}$ of $I_{\mathrm{PT}}(t)$.

$$n_e \approx \frac{d\hat{I}\sqrt{m_e}}{q_0^{3/2}\sqrt{2U}}\,, \tag{2.3}$$

where m_e and q_0 are the electron mass and charge, and U is the voltage applied to the electrode gap d. As the time period of the electron transit is of similar magnitude as the laser pulse duration, the n_e determined from (2.3) must be considered a lower limit to the real number of photoelectrons.

Photocurrent pulse in gas

As the electron motion is governed by their collisions with the gas particles, the electrons drift with a constant average velocity in the applied homogeneous electric field. Their drift velocity is a function

Table 2.1.: Characteristic mean photon absorption length σ of thin films for $\lambda = 245$ nm and $\lambda = 437$ nm.

material	σ_{245}	σ_{437}
Au	$8.3 - 8.6$ nm	$11.7 - 12.1$ nm
Pd	$8.6 - 8.9$ nm	$7.3 - 7.5$ nm

of E/N. The swarm displacement currents $I_{\mathrm{PT}}(t)$ are evaluated with a standard PT technique [28, 29, 41] in order to obtain n_e.

2.3. Results

Several different samples have been produced with a photo-active film of gold (Au), palladium (Pd), tungsten (W), or molybdenum (Mo). The film thickness was varied in a range between 10 and 15 nm.

The samples were investigated for their transmission spectrum and the photocurrent spectrum. Selected samples were further analysed in the PES under vacuum conditions, 10^{-5} Pa, and at elevated pressure. It should be noted that the photo-active films are covered by an adsorbance layer of residual gas under vacuum conditions. However, we measured steady parameter values, and we assume that the film surfaces have reached a state of equilibrium.

2.3.1. Transmission spectra

Using the HBO, the transmission of the samples has been recorded for those wavelengths λ which correspond to the Hg emission lines. Figure 2.4 presents the transmission spectra of selected samples.

The transmission as a function of the film thickness was evaluated for the mean absorption path σ using the Beer-Lambert law. The σ-results of Au and Pd are listed in table 2.1.

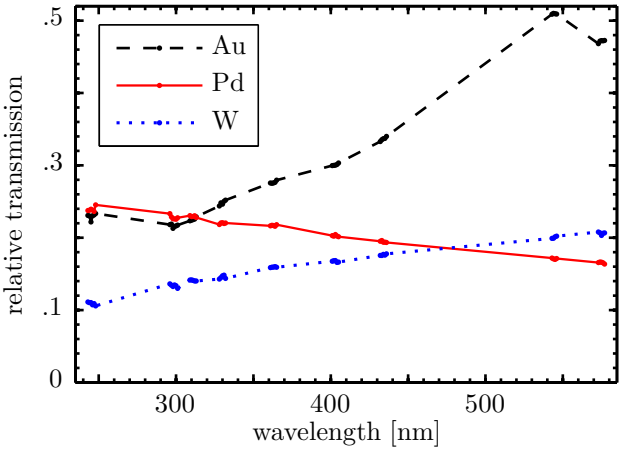

Figure 2.4.: Transmission spectra of selected metal films of 13 nm thickness. The lines are merely for guiding the eye.

2.3.2. Photocurrent spectra

Using the XBO, the photocurrent $I_{\mathrm{ph}}(\lambda)$ has been recorded as a function of λ. The shape of $I_{\mathrm{ph}}(\lambda)$ was analyzed, using the expansion of the Fowler function (6) and (7) from [32], in order to obtain Φ. For selected samples, the photocurrent spectra are shown in figure 2.5 together with the corresponding curves obtained from the Fowler function. The results of Φ are listed in table 2.2.

2.3.3. Pulsed operation

A temporal profile of the laser pulse was recorded, using a phototube in combination with the amplifier of the PT setup. The cumulative integral of the pulse response was calculated in order to obtain the corresponding step response [42], which is presented in figure 2.6 in arbitrary units.

In the PT setup, we recorded the current response of the electrical circuit to a laser pulse. Under vacuum conditions, with $d = 27$ mm, $U = 2$ kV, the pulse response has been recorded, using the oscil-

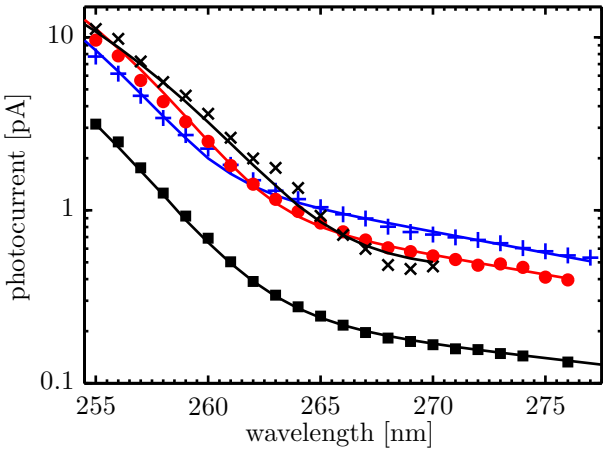

Figure 2.5.: Photocurrent spectra of a 13 nm Au film (■), and of Pd films with thickness 10 nm (+), 13 nm (•), and 15 nm (×). The lines (——) represent a fit of the Fowler function [32].

Table 2.2.: Results of the electron work function Φ for selected film materials (film thickness is given in brackets). QE_0 is the photocathode efficiency at 245 nm in vacuum. QE_{eff} are efficiencies measured in gases at 266 nm, with the lower value corresponding to 2 kPa, 20 Td, and the higher value to 10 kPa, 140 Td.

material		QE_0	$QE_{eff} \times 10^{-7}$	
(nm)	Φ /eV	$\times 10^{-5}$	in N_2	in CO_2
W (13)	$4.85 \pm .05$			
Mo (13)	$5.24 \pm .06$			
Au (13)	$4.80 \pm .04$	1.7	$0.29 - 0.37$	$2.4 - 3.3$
Pd (10)	$4.77 \pm .05$	1.3	$2.0 - 7.4$	$1.0 - 2.1$
Pd (13)	$4.74 \pm .04$	2.4		$1.1 - 1.8$
Pd (15)	$4.70 \pm .05$	0.89	$3.9 - 6.9$	$2.5 - 4.0$

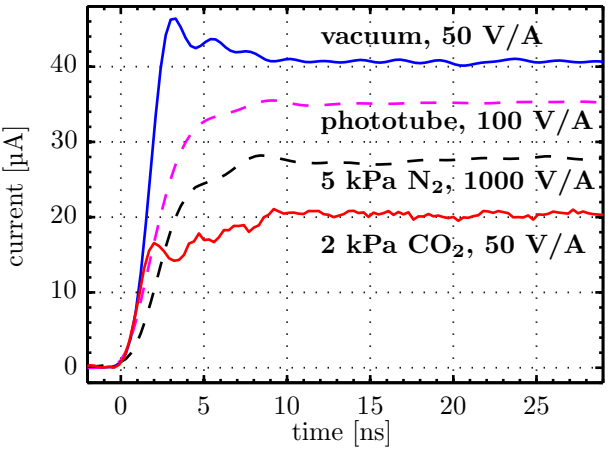

Figure 2.6.: Integrated pulse response of photoelectron current in vacuum (——), integrated laser pulse profile (– – –), and step responses of the swarm currents in N_2 (– – –) or CO_2 (——). The V/A-coupling of the oscilloscope or the amplifier is stated.

loscope coupling 50 V/A, i.e. without the amplifier. We found a peak current amplitude of 12 mA. Figure 2.6 shows the cumulative integral of this pulse response in arbitrary units.

A step response of the PT setup has been observed in the presence of a sample gas. In figure 2.7 two current waveforms are presented which have been recorded in argon sample gas. Figure 2.6 presents two current waveforms of swarms with approximately constant electron number, which have been measured with the following experimental settings:

1. N_2 5.0 kPa, 110 kV/m, amplification 1000 V/A.

2. CO_2 1.9 kPa, 27 kV/m, 50 V/A (without amplifier).

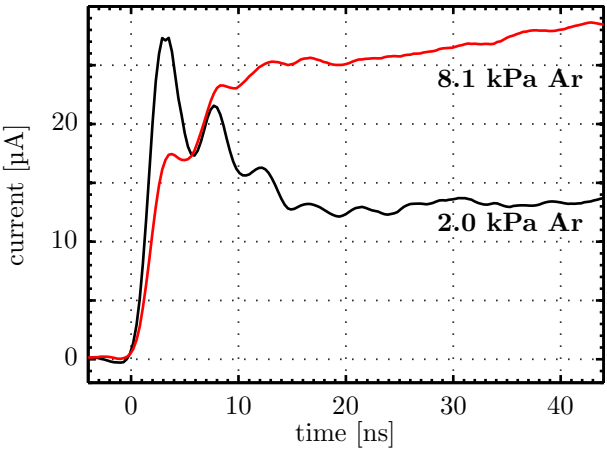

Figure 2.7.: Onset of the swarm currents in Ar, with E/N = 38 Td and amplification 1000 V/A.

2.3.4. Quantum efficiencies

The intensity of the HBO illumination was determined for the Hg emission lines near 245 nm, and the corresponding photocurrents have been measured for various Au and Pd samples in vacuum. Table 2.2 lists the resulting quantum efficiencies QE_0.

Various Au and Pd samples have been investigated in the PT setup in the presence of N_2 or CO_2. The gas pressure p was varied between 1 and 10 kPa, and E/N was varied between 20 and 140 Td. We recorded the swarm drift currents and determined the number of swarm electrons, using the method given in section 2.2.4, thus we determined the quantum efficiency QE_{eff} of the PES. It was found that QE_{eff} increases with increasing E/N and with increasing p. Table 2.2 gives the ranges of the observed QE_{eff}-values.

2.3.5. Long-term operation

One sample, a Pd film of thickness 13 nm, remained in the PT setup for many days and was alternatively kept in vacuum or operated in

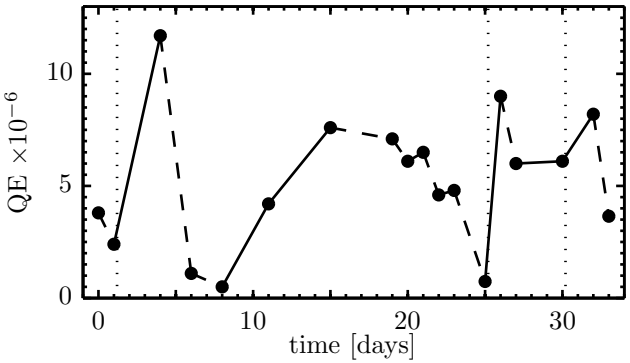

Figure 2.8.: Evolution of QE_0 for $\lambda = 266$ nm of a Pd (13 nm) sample during many days of intermittent operation in the PT setup. (——) indicates the periods under vacuum, (– – –) means operation in gases during that period. Vertical lines (· · · · · ·) represent the instants when the sample was flushed with H_2.

the gases N_2, CO_2 or SF_6. We repeatedly determined QE_0 from photocurrent pulses in vacuum, using (2.3). At selected instants, the sample photocathode was exposed to H_2 for a few minutes, and afterwards the H_2 was pumped out of the vacuum chamber. Figure 2.8 presents these QE_0-results.

2.4. Discussion

Our results indicate that Au and Pd films have very similar optical properties in the spectral range 250 nm $\leq \lambda \leq$ 300 nm; the two film materials approximately agree in the transmissivity, Φ and QE_0.

An important difference between Au and Pd photocathodes appeared due to an operation in the presence of N_2, where the QE_{eff} of Au photocathodes was found to collapse, see table 2.2. Probably, the decrease of QE_{eff} is caused by reactions on the Au surface between adsorbed species and N_2^+ or N_2 metastables.

2.4.1. Characteristics of transmissive Pd photocathodes

For Pd films of 10 to 15 nm thickness, the UV transmissivity is about 25%. For the PT application, it should be kept in mind that residual UV photons also travel along the path of the electron swarm. However, we note that even more photons do so in a reflective configuration.

It looks like small variations, ±2 nm, of the film thickness are uncritical for implementing transmissive photocathodes, because the magnitude of photocurrents depends only weakly on the film thickness (see figure 2.5). We note that it is feasible to assess the film homogeneity and thickness by transmitting green light.

As table 2.2 shows, a QE_0 of 1 to 2 $\times 10^{-5}$ was found for $\lambda =$ 245 nm in vacuum. For $\lambda = 266$ nm, the QE_0 can also exceed 10^{-5} in vacuum, as one can note from figure 2.8. It must be emphasized that Φ is very similar to the photon energy of the laser, $\epsilon_p = 4.66$ eV. When Φ varies due to a change in the surface conditions of the photocathode (see section 2.1.3), a large change can occurr in the QE. Figure 2.8 shows how QE_0 slowly degrades during an operation in gases. The QE_0 can be slowly restored while the photocathode is being kept in vacuum after contamination.

Figure 2.8 demonstrates a dramatic increase of QE_0 after the photocathode was flushed with H_2. After a hydrogenization had been performed, the residual pressure in the vacuum chamber increased by about 4×10^{-6} Pa. Thus, we observe only a minor outgassing of H_2, and we can exclude a substantial pollution of the gas samples. However, one should keep in mind the occurrence of chemical reactions mentioned in section 2.1.3.

2.4.2. Characteristics of the PES

A step response of the vacuum photocurrent (figure 2.6) has a very short risetime of 3 ns. That duration corresponds to the principal emission of the laser pulse. From the laser pulse profile, one can see that 90% of the laser pulse energy is emitted within 4 ns duration.

Table 2.3.: The time duration τ_{eq} which the electron swarm takes to attain hydrodynamic equilibrium.

gas	p (kPa)	τ_{eq} (ns)	E/N (Td)
Ar	8.1	13	38
Ar	2.0	20	38
CO_2	2.0	9	58
N_2	5.0	10	90

No laser light was detectable 8 ns after the onset of a pulse.

The vacuum photocurrent shown in figure 2.6 has a much larger amplitude than the electron swarm currents expected in the present PT setup. Such high currents served for testing the transient electrical behaviour of the PT setup. As figure 2.6 shows, there is a 10% overshooting of the step response, and minor oscillations appear for a period of 6 ns after the end of the electron transit. Altogether, there is a time duration of 10 ns between the onset of laser emission and the decay of oscillations in the circuit. When the amplifier is used with a setting of 100 V/A or 1000 V/A, a settling time of the step response of 10 ns is apparent from figure 2.6. This demonstrates that the amplifier bandwidth is adequate for resolving the electron swarm currents in the present PT setup.

2.4.3. Swarm equilibration

As $\varepsilon_p \approx \Phi$, the photoelectrons have an initial energy close to 0 eV. They are accelerated by the electric field, which is the sum of the externally applied field, and the field of the space and images charges. In a steady equilibrium, the swarm electrons have a mean energy of a few eV. Obviously, the electron swarm can reach a state of equilibrium only after having travelled for a certain time period and for a certain distance away from the photocathode. For example in CO_2 (figure 2.6), the swarm current amplitude increases *after* the princi-

pal laser emission to reach a plateau at the instant $\tau_{eq} \approx 9$ ns. The constant swarm current for $t > 9$ ns corresponds to an equilibrated swarm. In table 2.3 the time to equilibrium τ_{eq} is listed for selected gas species and pressure values.

Figure 2.7 indicates a strong influence of the gas pressure on the initial evolution of electron swarms in Ar. For $p = 8$ kPa, the swarm current reaches a plateau of 25 µA after 12 ns. In contrast, for $p = 2$ kPa, there is a strong initial increase of the swarm current, but then it decreases to reach a plateau of 13 µA after ∼20 ns. Such a current decrease is consistent with a loss of swarm electrons to the photocathode because they are back-scattered in elastic collisions with Ar. Strong oscillations of the swarm current are observable for $p = 2$ kPa, however, the oscillation amplitude is much smaller for $p = 8$ kPa. In an SST arrangement, spatial oscillations of electron currents were previously found in the immediate vicinity of the cathode in the rare gases [43–45], and in N_2 [46]. Observing light emissions from SST discharges, Fletcher showed [43] that these oscillations are not an artifact of the electrical detection method. The oscillatory structures arise from the repeated, spatially discrete onset of inelastic collisions of not yet equilibrated electrons [45, 46].

As one can note from figure 2.7, the number of initial swarm electrons increases with increasing p in Ar for constant E/N, for a particular laser intensity and slowly varying photocathode efficiency. Likewise, in N_2 and CO_2 the initial number of swarm electrons depends on the choice of p and E/N for a particular laser intensity, as it is apparent from table 2.2.

2.5. Conclusions

A pulsed electron source was successfully implemented in a pulsed Townsend setup. It was characterized for the photoelectric properties and the transient electrical behaviour. Electron displacement currents can be recorded with high fidelity, and it was feasible to observe their evolution immediately after the electron ensemble had

been initiated at the photocathode. We gave, probably for the first time, direct evidence of oscillating swarm currents, which represent the temporal counterparts of the spatial current oscillations well known from the famous Franck-Hertz [45] experiment.

The present design of a photocathode provides a robust electrical bonding. A photocathode mount was presented that can be conveniently loaded into the electrode system of the application. The geometry of the photocathode mount allows for a precise alignment with the electrodes, in order to reduce a disturbance of the homogeneous electric field between the electrodes.

We showed that a transmissive palladium photocathode is well suited for pulsed Townsend applications. It provides a useful performance during many hours of uninterrupted operation in the presence of gases. The palladium photocathode can be repeatedly cleaned by applying H_2. Thus, the efficiency of the photocathode can be restored in situ when it has been polluted.

During an operation in the presence of gases, the efficiency of the electron source depends on the set values of N and E/N for a given laser pulse energy. Moreover, the work function of the photocathode can slowly vary in the course of a measurement sequence. In order to perform a measurement sequence with a constant number of initial swarm electrons, the laser pulse energy should be adjusted to counteract efficiency variations of the electron source.

3. Pulsed Townsend method and signal processing

This chapter is based on a published article [41].

3.1. Introduction

Measurements of electron swarm parameters in gases are required for basic studies of electron kinetics and electron-atom or electron-molecule interactions [10], and are essential for simulations of plasma devices [20, 47, 48]. The pulsed Townsend (PT) method is a traditional experiment for measuring electron swarm parameters [10, 21]. Its main advantages are that it permits direct observation of the spatiotemporal evolution of an electron swarm yielding ionization and electron drift and diffusion data at the same time. The operation of a PT experiment involves several repetitive tasks in between measurements, which consume more time than the measurement itself. We have built the SParX (swarm parameter experiment) PT setup using dedicated control software for running measurements in automated processes. These techniques permit quick coverage of multi-dimensional parameter spaces, such as different mixing ratios of dual and ternary gas mixtures.

The analysis of PT measurements is based on the time dependent Gaussian spatial distribution of swarm electrons [21]

$$\frac{\mathrm{d}n_\mathrm{e}(z,t)}{\mathrm{d}z} = \frac{n_0 \exp\left(\alpha_\mathrm{eff} z\right)}{\sqrt{4\pi D_\mathrm{L} t}} \exp\left(-\frac{(z-wt)^2}{4D_\mathrm{L} t}\right) , \tag{3.1}$$

where α_eff is the effective ionization coefficient, D_L is the diffu-

sion coefficient in the z-direction, w is the swarm velocity in the z-direction, and n_0 is the electron number at $t = 0$ and $z = 0$. This Gaussian electron density distribution is formed by an equilibrated swarm in unbound space [49], even if the electron energy distribution is spatially dependent [50].

However, in the PT method the parameters α_{eff} and D_{L} can not be determined directly without precise knowledge of z. Moreover, there is pertinent discussion about the interpretation of PT measurements, perhaps because the relation between the PT method and theoretical quantities of electron transport was considered for special cases only [19, 51], but not universally.

A different evaluation procedure is applied here. This chapter begins with a transformation of (3.1). It yields an expression $n_{\mathrm{e}}(z, t)$, where the parameters are time intervals and frequencies. Waveforms of PT measurements can then be analyzed without a priori assuming values z and w, and it is possible to develop regression analyses for obtaining the electron swarm parameters. Subsequent sections present details of the experimental setup and measurement procedures. Briefly we review the available reference data of Ar, N_2 and CO_2, then our results for these gases are presented and compared to those of the references.

3.2. Model of electron swarms and their currents

The kinetic theory of swarms is found e.g. in reviews by Kumar [10] or Petrović [20]. On the basis of kinetic theory, the PT method was described by a temporal electron growth [18, 19, 51]. It is necessary to transform the spatial swarm model (3.1) to the temporal domain using the relations

$$\alpha_{\mathrm{eff}} \mathrm{d}z = \nu_{\mathrm{eff}} \mathrm{d}t \tag{3.2}$$

$$2D_{\mathrm{L}} t = w^2 \tau_{\mathrm{D}} t \,, \tag{3.3}$$

which introduce the effective reaction rate ν_{eff} and the diffusion time constant τ_{D}. Inserting these relations in (3.1) yields

$$\frac{\mathrm{d}n_{\text{e}}(z,t)}{\mathrm{d}z} = \frac{n_0 \exp\left(\nu_{\text{eff}} t\right)}{w\sqrt{2\pi\tau_{\text{D}} t}} \exp\left(-\frac{(t-T)^2}{2\tau_{\text{D}} t}\right) . \tag{3.4}$$

With

$$w = \frac{\mathrm{d}z}{\mathrm{d}t} \tag{3.5}$$

one obtains a temporal electron number distribution $\mathrm{d}n_{\text{e}}/\mathrm{d}t$ with its peak at the instant $T = z/w$.

3.2.1. Model of electron swarms

At an arbitrary position $z = d_0$ an initial electron distribution is assumed,

$$\frac{\mathrm{d}n_e(d_0,t)}{\mathrm{d}t} = \frac{n_0}{\sqrt{2\pi\sigma_0^2}} \exp\left(-\frac{(t-t_0)^2}{2\sigma_0^2}\right) , \tag{3.6}$$

with initial electron number n_0 and initial temporal broadening σ_0. At the instant t_0 is the center of the Gaussian laser pulse. This swarm moves at constant average bulk velocity w, and, after the transit time T, passes an observer at position $d = d_0 + wT$. There the electron distribution is

$$\frac{\mathrm{d}n_{\text{e}}(d,t)}{\mathrm{d}t} = \frac{n_0 \exp\left(\nu_{\text{eff}}(t-t_0)\right)}{\sqrt{2\pi\sigma^2(t)}} \exp\left(-\frac{(t-t_0-T)^2}{2\sigma^2(t)}\right) . \tag{3.7}$$

The swarm temporal broadening $\sigma(t)$ increases with the diffusion time constant τ_{D}.

$$\sigma^2(t) = \sigma_0^2 + \tau_{\text{D}}(t-t_0) \tag{3.8}$$

The total number of electrons changes at an effective rate ν_{eff}, which accounts for electron attachment and ionization. The model collapses with electron detachment, cathodic feedback or photoionization by secondary photons. However, ν_{eff} is not affected by ionic or metastable species *accumulated* in the gas, because their residence time is shorter than the interval between two subsequent measurements.

3.2.2. Electron currents

An analytical expression of the swarm drift current is deduced and serves for comparison to measured currents. Similar expressions for electron currents were given by de Urquijo [52] and Ridenti [53] and have elsewhere been used for analysing PT measurements.

The electron current $I_{\mathrm{e}}(t)$ of a swarm that moves across an electrode gap d and has a transit time T is proportional to the number of electrons in the gap [54].

$$I_{\mathrm{e}}(t) = \frac{q_0}{T} \int_0^d \frac{\mathrm{d}n_{\mathrm{e}}(z,t)}{\mathrm{d}t}\,\mathrm{d}z\ , \tag{3.9}$$

where q_0 is the electron charge. $I_{\mathrm{e}}(t)$ can be expressed as the product of a constant amplitude and three time dependent amplitude factors [52, 53].

$$I_{\mathrm{e}}(t) = \frac{n_0 q_0}{T}\,\frac{1+A_{\mathrm{L}}(t)}{2}\,\frac{1-A_{\mathrm{D}}(t)}{2}\,A_\nu(t) \tag{3.10}$$

$A_{\mathrm{L}}(t)$ accounts for the swarm initiation in front of the cathode, $A_{\mathrm{D}}(t)$ accounts for the absorption of the swarm at the anode, and

$$A_\nu(t) = \exp\left(\nu_{\mathrm{eff}}(t-t_0)\right)\ . \tag{3.11}$$

An ensemble of photoelectrons is initiated at position d_0 in front of the cathode by a laser pulse of Gaussian temporal profile, and it is accelerated in the electric field. We assume that the laser pulse

profile determines the electron swarm for the times $t \leq t_0$, and that the effect of diffusion begins at the instant t_0. Then the amplitude factor $A_\mathrm{L}(t)$ can be defined using the canonical error function erf.

$$A_\mathrm{L}(t) = \begin{cases} \mathrm{erf}\left(\frac{t-t_0}{\sqrt{2\sigma_0^2}}\right) & \text{for } t \leq t_0 \\ \mathrm{erf}\left(\frac{t-t_0}{\sqrt{2\sigma_0^2+2\tau_\mathrm{D}(t-t_0)}}\right) & \text{for } t > t_0 \end{cases} \tag{3.12}$$

For an electrode gap $d = d_0 + wT$ the amplitude factor $A_\mathrm{D}(t)$ is

$$A_\mathrm{D}(t) = \mathrm{erf}\left(\frac{t - t_0 - T}{\sqrt{2\sigma_0^2 + 2\tau_\mathrm{D}(t-t_0)}}\right) . \tag{3.13}$$

The experimental conditions can be chosen such that T is much larger than τ_D. Then $A_\mathrm{L}(t)$ can be evaluated when $A_\mathrm{D} = -1$, and $A_\mathrm{D}(t)$ can be evaluated when $A_\mathrm{L} = 1$. When $A_\mathrm{D} = -1$ and $A_\mathrm{L} = 1$, then $A_\nu(t)$ can be evaluated independently of initial broadening and diffusion.

3.2.3. Ion currents

In the present investigation only electron currents $I_\mathrm{e}(t)$ are analysed, but in many cases substantial ion currents are observed after the electron transit. Then ions are also present during the electron transit, and it is essential to separate the ion current $I_\mathrm{ion}(t)$ from $I_\mathrm{e}(t)$:

$$I_\mathrm{measured}(t) = I_\mathrm{e}(t) + I_\mathrm{ion}(t) \tag{3.14}$$

A simple expression of $I_\mathrm{ion}(t)$ is used. For the times $t_0 \leq t \leq T + t_0$ it is

$$I_\mathrm{ion}(t) = \begin{cases} A_\mathrm{ion}\,\frac{t-t_0}{T} & \text{for } \nu_\mathrm{eff} \leq 10^3/\mathrm{s} \\ A_\mathrm{ion}\,\frac{\exp(\nu_\mathrm{eff}(t-t_0))-1}{\exp(\nu_\mathrm{eff}T)-1} & \text{for } \nu_\mathrm{eff} > 10^3/\mathrm{s}\,, \end{cases} \tag{3.15}$$

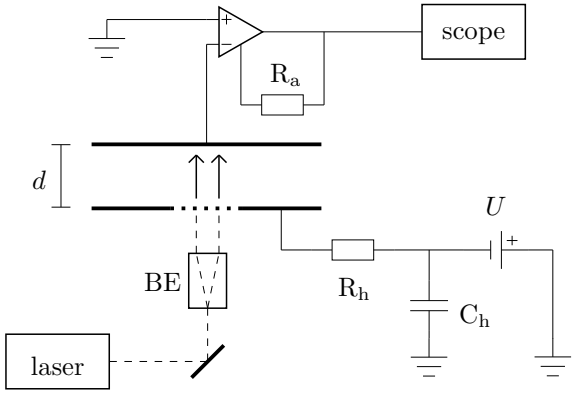

Figure 3.1.: Optical setup and electric circuit diagram. The two electrodes with spacing d are within a vacuum chamber. The laser beam (– – –) illuminates the photocathode (· · · · · ·) via a beam expander (BE). Arrows indicate the swarm drift direction. High voltage elements are the DC source U, damping capacitance C_h and resistance R_h. The anode is connected to the oscilloscope via a transimpedance amplifier with variable gain R_a.

and for $t > T + t_0$ it is

$$I_{\text{ion}}(t) = A_{\text{ion}} \ , \tag{3.16}$$

where A_{ion} is the ion current amplitude at the end of the electron transit.

3.3. Experimental setup and evaluation methods

3.3.1. Pulsed Townsend setup and operation

The experiment is installed in a cylindrical stainless steel vacuum ($< 10^{-5}$ Pa) chamber. After the inflow of sample gases is completed, the gas temperature is measured by a Pt100 sensor, and the pressure is measured by a capacitive sensor for the range 50 Pa to 11 kPa.

In the chamber two polished stainless steel electrodes with radius $r_0 = 56$ mm represent a $(\pi/2)$-Rogowski geometry for their ideal spacing $z_0 = 15$ mm. The parametrization of their profile (r, z) is

$$r = [0 \dots r_0] \tag{3.17}$$

$$z(r) = \frac{z_0}{\pi} \exp\left(2.35 - \frac{r_0 - r}{z_0/\pi}\right) . \tag{3.18}$$

This electrode geometry produces an electric field of cylindrical symmetry that is almost homogeneous for $r < 20$ mm with $d \leq 18$ mm, and it limits the field strength at the electrode edges. The z-position of the anode, and thus the electrode spacing d, can be varied by a motor driven micrometer screw in steps of 6 µm.

Centrally in the cathode a plane photocathode with diameter 25 mm is installed, which was described in chapter 2. The film is back-illuminated, as indicated in figure 3.1, by 266 nm laser pulses of 1.5 ns FWHM and about 155 µJ pulse energy at 20 Hz repetition rate, producing about 3×10^7 initial swarm electrons. The laser beam is expanded to cover the complete photocathode. We were able to choose this simple and economic laser system (CryLas FQSS 266-200) because the photocathode is so very efficient.

Figure 3.1 shows the electric circuit that contains the electrodes. We use damping elements $R_h = 150\ \Omega$ and $C_h = 2.7$ µF between the DC high voltage source and the cathode. The low voltage circuit was optimised for high signal bandwidth (200 MHz) and high fidelity. The anode is connected to a transimpedance amplifier (FEMTO DHPCA-100) with gain resistor R_a. For recording electron currents we set $R_a = 10^2$ or 10^3 V/A, and ion currents can be recorded with $R_a = 10^5$ or 10^6 V/A. The oscilloscope (R&S RTO) is equipped with a 10 GS/s 8 bit AD-converter and a 16 bit digital signal processor, which is configured for data compression and averaging. It is triggered by a photodiode built into the laser system.

The operation of all elements of the setup is remotely controlled and has been integrated into a single Matlab environment on a control computer.

Range and uncertainty of experiment parameters

The experiment operates at gas temperatures 293 to 300 K which are measured but not controlled. E/N is controlled by the experimental parameters d, p, U. For the present study their range of values is:

- d from 9 to 18 mm.
- p from 1 to 11 kPa (N from 0.27 to 3×10^{24} m^{-3}).
- U up to 6 kV.

The uncertainty of the absolute electrode spacing is ±200 µm, but care was taken that the relative electrode spacing can be controlled reproducibly to ±6 µm. Due to the regression methods described below, reproducibility of setting U and p is not important. The uncertainty of absolute (E/N)-values depends on the *relative* error of the U-, p- and temperature-measurements, and on the uncertainty of electrode spacing. In the present setup the uncertainty of E/N is ±1.5% typically.

3.3.2. Analysing electron currents

Two examples of current waveforms are shown in figure 3.2. The initial broadening of the swarm σ_0 and its starting time t_0 are obtained by fitting (3.6) to the time derivative of the rising edge of the waveform. A tentative fit of (3.10) with four free parameters to the whole waveform produces preliminary values $n_0, T, \nu_{\text{eff}}, \tau_{\text{D}}$. Using these preliminary values, the waveform is partitioned into intervals which are analysed individually. The ion current amplitude A_{ion} is determined at T_4, and the ion current $I_{\text{ion}}(t)$ is subtracted from the waveform using (3.15). The electron current $I_{\text{e}}(t)$ is analysed by fitting expressions of only two free parameters. From the interval T_1 to T_2, as shown in figure 3.2, the definitive values n_0 and ν_{eff} are determined. This allows the injected electrons to settle to an equilibrium state (see also sections 3.3.4 and 3.6.1), and eliminates the

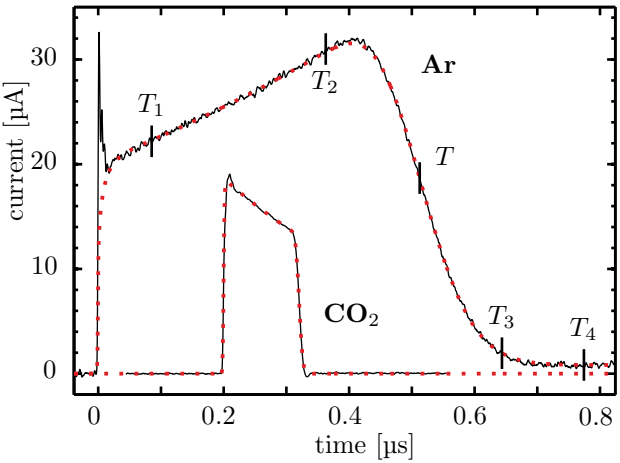

Figure 3.2.: Swarm drift currents in Ar at 30 Td and in CO_2 at 65 Td, the latter current was divided by 10 and time shifted by 0.2 µs. Averages of measured waveforms (——) and the fit (·····) of (3.10) coincide well. T marks the electron transit time in Ar, and the markers T_1 to T_4 are explained in section 3.3.2.

influence of minor field inhomogeneities at the cathode. Another fit to $I_e(t)$ between T_2 and T_3 produces T and τ_D.

This analysis relates one set of waveform parameters (T, ν_{eff}, τ_D) to one set of experimental parameters (N, d, U).

3.3.3. Algorithm of measurement sequence

A particular gas sample is examined systematically in a sequence of measurements. For various settings of the experiment parameters (N, d, U), current waveforms are sampled. Typically, a certain value E/N is implemented for several different combinations of (N, d, U). For the presently adopted procedures, the admissible (E/N)-range is limited. A minimum value $(E/N)_{min}$ is required for obtaining a measurable current amplitude, and an upper limit $(E/N)_{max}$ is reached when [ionization is strong, and substantial ion currents are observable]. The value $(E/N)_{min}$ is determined by the experimentor prior to starting the measurement sequence, but $(E/N)_{max}$ is a priori unknown, and it depends on Nd and on the sample gas. However, the algorithm of the measurement sequence requires a termination criterion, which can be defined as a maximum number of electrons $n_{max} \approx 10^8$ at the end of electron transit. Whenever n_{max} is observed the algorithm has reached the upper limit $(E/N)_{max}$ and terminates the sequence.

In principle the algorithm consists of three nested loops. The outer loop iterates over a list of gas concentrations $N_1..N_{end}$, the second loop iterates over a list of electrode distances $d_1..d_{end}$. In the inner loop the voltage U is set, then a current waveform is recorded and analysed for the number of electrons, which arrive at the anode. Initially the inner loop implements $(E/N)_{min}$, and iteratively U is increased. The inner loop terminates when n_{max} is exceeded.

Typically, one sequence consists of measurements at four d-values and four N-values, and one obtains about two hundred current waveforms which are analysed individually.

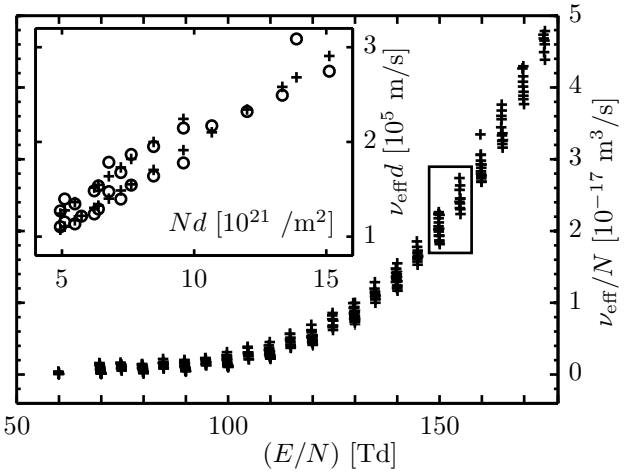

Figure 3.3.: Individual values of effective ionization rates $\nu_{\rm eff}$ of one measurement sequence for N_2. The box near 150 Td marks the values that appear in the inset. The inset shows the measured (◯) and fitted (+) values in the regression of $\nu_{\rm eff}d$ over Nd for obtaining $\nu_{\rm eff}/N$ at 152.5 Td.

3.3.4. Regression and normalization of swarm parameters

Paschen's relation states that all swarms are similar under the condition Nd = const. Then $\nu_{\rm eff}$ and $\tau_{\rm D}$ can be normalized by the gas density N for obtaining the temporal swarm parameters $\nu_{\rm eff}/N$ and $N\tau_{\rm D}$. These swarm parameters only depend on E/N for one particular gas mixture.

When swarm parameter data are produced by normalizing and averaging measurements at similar E/N, possible offsets or systematic disturbances of the measured quantities can manifested themselves in the results. In order to overcome these drawbacks, regression methods have been developed for obtaining w and $D_{\rm L}$ from time-of-flight measurements [55]. The present swarm model permits regression analyses to be applied also to PT measurements. The approach is further generalized to facilitate a simultaneous evaluation of mea-

surements at different N and slightly different (E/N)-values.

For this section, we introduce the abbreviations $R = \nu_{\text{eff}}/N$ and $D = N\tau_{\text{D}}$, and the subscript is omitted from ν_{eff} in order to improve the readability of equations.

Be $(E/N)_0$ an arbitrary value within the E/N-range of the measurement sequence, and be $\Delta_{\text{E/N}}$ much smaller than $(E/N)_0$. Then there are J sets of measured quantities from the sequence between $(E/N)_0 - \Delta_{\text{E/N}}$ and $(E/N)_0 + \Delta_{\text{E/N}}$,

$$(N_j,\, d_j,\, (E/N)_j,\, T_j,\, \nu_j,\, \tau_{\text{D}j})\ ,\ j = 1, .., J\ . \tag{3.19}$$

These J sets are treated in three independent analyses for obtaining the values w_0, R_0, D_0 at $(E/N)_0$. An example of the selection and regression procedure is given in figure 3.3.

Swarm velocity w

We assume that w depends linearly on E/N in the selected very narrow E/N-range.

$$w_j = w_0 + \mathrm{d}w\ [(E/N)_j - (E/N)_0] \tag{3.20}$$

This dependence is inserted into (3.5) for obtaining a linear regression of d_j on T_j, which is a generalization of the usual difference method of time-of-flight experiments.

$$d_j = T_j \left\{ w_0 + \frac{\mathrm{d}w}{\mathrm{d}(E/N)}\ [(E/N)_j - (E/N)_0] \right\} + d_0\ , \tag{3.21}$$

From (3.21) the value of the swarm velocity w_0 and its tangent $\frac{\mathrm{d}w_0}{\mathrm{d}(E/N)}$ at $(E/N)_0$ can be obtained. The constant term d_0 in (3.21) accounts for the measurement uncertainty of the gap distance and for the fact, that the swarm is only initiated immediately in front of the cathode and equilibrates during the initial drift, as it was pointed out by Townsend [56].

Effective reaction rate ν_{eff}/N

For all the distances d_j one can write

$$\nu_j d_j = R N_j d_j \ . \tag{3.22}$$

Equation (3.22) states that the validity of Paschen's similarity relation also implies that $\nu_{\mathrm{eff}} d = \mathrm{const}$ is a similiarity relation of electron swarms.

When R is a linear function of E/N in the selected small interval, the regression equation for R_0 at $(E/N)_0$ is

$$\nu_j d_j = N_j d_j \left\{ R_0 + \frac{\mathrm{d}R}{\mathrm{d}(E/N)} \left[(E/N)_j - (E/N)_0 \right] \right\} + (\nu d)_0 \ , \tag{3.23}$$

from which the tangent $\frac{\mathrm{d}R}{\mathrm{d}(E/N)}$ at $(E/N)_0$ is also obtained. As in (3.21) a constant term $(\nu d)_0$ is included.

Diffusion time $N\tau_{\mathrm{D}}$

The considerations, which lead to (3.21) and (3.23), also apply for D.

$$\frac{\tau_{Dj}}{d_j} = \frac{D}{N_j d_j} \tag{3.24}$$

Expression (3.24) implies the similarity relation $\tau_{\mathrm{D}}/d = \mathrm{const}$, and it defines the regression equation for D_0

$$\frac{\tau_{\mathrm{D}j}}{d_j} = \frac{D_0 + \frac{\mathrm{d}D}{\mathrm{d}(E/N)} \left[(E/N)_j - (E/N)_0 \right]}{N_j d_j} + (\tau_{\mathrm{D}}/d)_0 \ , \tag{3.25}$$

and the tangent $\frac{\mathrm{d}D}{\mathrm{d}(E/N)}$. The constant term $(\tau_{\mathrm{D}}/d)_0$ is due to the initial broadening of the electron swarm, for which the laser pulse duration is one reason. As pointed out by Wetzer [42], the deviation of the electrodes from parallel alignment gives also rise to an offset in the measurement of τ_{D}.

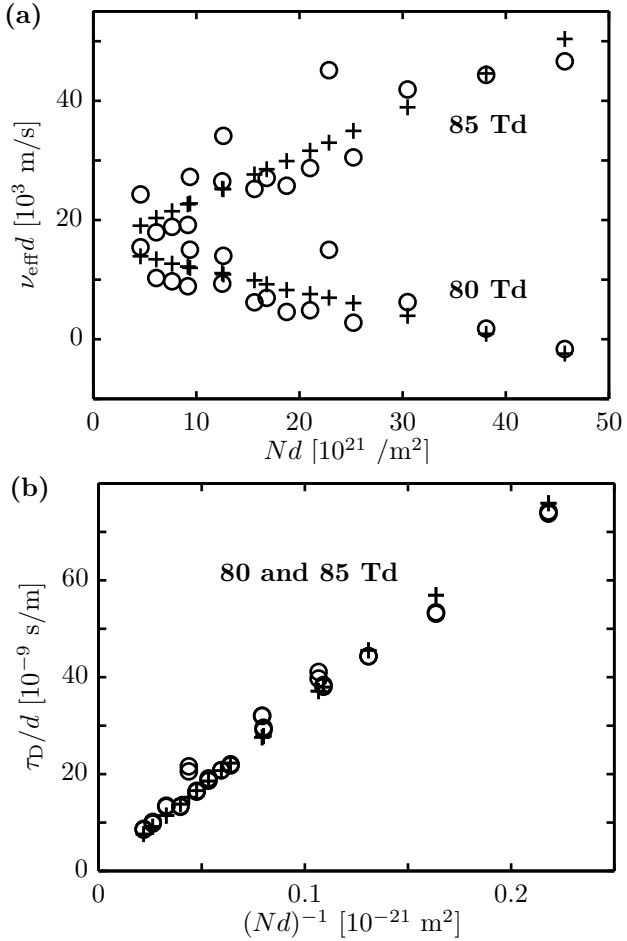

Figure 3.4.: Measured (◯) and fitted (+) values in the regression analyses for CO_2, which include measurements at 80 and 85 Td. (a) regression of $\nu_{\rm eff}d$ over Nd used for obtaining $\nu_{\rm eff}/N$ at 82.5 Td. (b) regression of $\tau_{\rm D}/d$ over $(Nd)^{-1}$ used for obtaining $N\tau_{\rm D}$ at 82.5 Td.

3.4. Benchmark data

Ar, N_2 and CO_2 were chosen for benchmarking our methods, because for these gases the electron drift velocity and ND_L have been measured with highest precision using time-of-flight methods [55, 57, 58], and because α_{eff}/N is well known from steady-state Townsend measurements [59, 60].

On the basis of these measurements, and including results from beam methods [15, 61], cross section sets were established for the benchmark gases [57, 62, 63], and their electron transport parameters can be calculated or simulated. The calculations of benchmark data were done with a Boltzmann solver using the two-term approximation (Bolsig+ [18] version 11.2011, settings: Precision 10^{-13}, Convergence 10^{-5}, Iterations 100, default SIGLO cross sections). Simulations were done with a Monte Carlo method (Magboltz [5] version 9.0.1, setting $4 \cdot 10^8$ real collisions, Biagi's cross sections). It has to be noted Magboltz can produce dedicated PT parameters for higher (E/N)-values, however, in the (E/N)-range of the present study the general transport coefficients must be used. We emphasize that Bolsig+ and Magboltz use different cross section sets.

In addition to calculated and simulated data, experimental reference data was considered, but the options were restricted to publications giving tabulated data. We selected the PT measurements by de Urquijo in N_2 [64]. Raju's compilation of swarm parameters [65], which was the most recent available to us, gives Haydon's α_{eff}/N for N_2 [59], and Bhalla's α_{eff}/N for CO_2 [60].

3.5. Measurements and evaluation of swarm parameters

Measurement sequences were made in Ar (purity 6.0) at pressures between 2.1 and 10.5 kPa, in N_2 (5.0) between 1.5 and 10.5 kPa. In CO_2 (5.0) we made an overview measurement with step-size 5 Td at pressures between 2.5 and 10.5 kPa. A second investigation of the

(E/N)-range 20 to 45 Td was done with step-size 1 Td at pressures between 5.0 and 9.1 kPa. The gas pressure and temperature (293 to 300 K) were simultaneously measured for every recorded waveform.

The measurements were carried out as described in section 3.3.3 and analysed individually according to the procedure given in section 3.3.2. For example, the sequence data of ν_{eff} in N_2 are presented in figure 3.3. The sequence data were then sampled using the regression methods of section 3.3.4 for obtaining w, ν_{eff}/N and $N\tau_{\text{D}}$. Both sequences of CO_2 have been merged and treated together by the regression analyses. Examples of regression analyses are presented in figures 3.3 and 3.4. Figure 3.4 includes measurements at 80 Td, where attachment dominates ($(\nu_{\text{eff}}/N) < 0$), and at 85 Td, where ionization dominates. Thus, two distinct branches are apparent in panel (a), one with positive and one with negative slope. In panel (b) two branches coincide, because electron diffusion is practically the same at 80 and 85 Td. The inset of figure 3.3 includes measurements at 150 and 155 Td, and two branches with slightly different slopes are discernible in the analysis used for obtaining ν_{eff}/N at 152.5 Td.

The evaluated swarm parameters of Ar, N_2 and CO_2 are listed in the appendix in tables A.1, A.5 and A.9, respectively. The 99% confidence intervals of the least-squares fit parameters were interpreted as statistical errors of the regression analyses. The tables include the statistical error of ν_{eff}/N, where it is larger than the rounding error. The statistical error of w is about $\pm 0.2\%$, and $\pm 2\%$ for $N\tau_{\text{D}}$. The uncertainty of the E/N values is $\pm 1.5\%$.

3.5.1. Presentation of results

In order to compare our results with the benchmark data, the electron flux velocity v_{d} and mobility μN were estimated from our w-data according to Tagashira's definition for TOF experiments [19].

$$\mu N = \frac{v_{\text{d}}}{E/N} = \frac{w}{E/N}\sqrt{1 - (\nu_{\text{eff}}/N)\,(N\tau_{\text{D}})} \tag{3.26}$$

Over the range of parameter values considered here (tables A.1, A.5 and A.9), the difference between v_d and w is generally $< 0.5\%$. Using v_d the effective ionization coefficient α_eff/N was estimated by

$$(\alpha_\mathrm{eff}/N) = \frac{\nu_\mathrm{eff}/N}{v_\mathrm{d}} \,. \tag{3.27}$$

Our electron mobilities μN and effective ionization coefficients α_eff/N are presented in figure 3.5, together with the reference data introduced in section 3.4.

The present $N\tau_\mathrm{D}$-results are shown in figure 3.6 as cubic spline curves, which were constructed from the $N\tau_\mathrm{D}$-data and from the tangents $\mathrm{d}(N\tau_\mathrm{D})/\mathrm{d}(E/N)$, as defined in (3.25). The ND_L-results of Bolsig+ and Magboltz were included in figure 3.6 using

$$N\tau_\mathrm{D} = \frac{2}{v_\mathrm{d}^2}\, ND_L \,. \tag{3.28}$$

The critical field strength $(E/N)_\mathrm{crit} = 81.6 \pm .9$ Td of CO_2 was determined from our data where ν_eff/N equals zero, and $(E/N)_\mathrm{crit} = 82.1 \pm .3$ Td was derived from Magboltz results.

3.6. Discussion

3.6.1. Waveforms

Figure 3.2 demonstrates in the current measurements strong effects of processes in the immediate vicinity of the cathode. These effects have been discussed in section 2.4.3. The swarm requires to travel for $10-20$ ns in order to attain a state of equilibrium. For $t > 20$ ns there is excellent agreement between measured currents and the ones derived from our swarm model.

3.6.2. Advantage of regression methods

ν_{eff}/N is supposed to approach zero for $(E/N) < 85$ Td in N_2, and for $(E/N) < 20$ Td in Ar. In these parameter ranges, our methods determined small negative ν_{eff}/N, as one can see from the tables A.1 and A.5. Such small (ν_{eff}/N)-values presumably correspond to the detection limit. Thus, the present methods permit measurements of ν_{eff}/N stronger than $\pm 5 \times 10^{-20}$ m^3s^{-1}.

In figure 3.4(a), the observed ν_{eff} are positive in the lower ν_{eff}-branch, for unknown reasons. If ν_{eff}/N was determined by averaging the values of the lower ν_{eff}-branch, then ν_{eff}/N would be positive for CO_2 at 80 Td, and one would conclude $(E/N)_{\text{crit}} < 80$ Td. However, our method determines ν_{eff}/N from the slope of the ν_{eff}-branches, and $(E/N)_{\text{crit}} = 81.6 \pm .9$ Td is obtained for CO_2. The regression method is especially well suited for determining $(E/N)_{\text{crit}}$ of the sample gas.

Diffusion time constants $N\tau_{\text{D}}$ are determined by the regression with statistical errors $\pm 2\%$, whereas averaging methods produce statistical errors in the order of $\pm 10\%$ for ND_{L} [64].

As the regression methods can produce local tangents, swarm parameters can be plotted as cubic spline curves, as it was done in figure 3.6, and the plot can be analyzed for data consistency. For example, in our $N\tau_{\text{D}}$-results of CO_2 between 30 and 40 Td, the tangents deviate from the slope of the global curve. An inconsistency of $N\tau_{\text{D}}$ appeared where the two measurement sequences have been merged.

3.6.3. Comparison to reference data and simulations

Ar

As shown in figure 3.5(a), our results of $\boldsymbol{\mu N}$ reproduce the values from Magboltz for $E/N < 35$ Td. For $(E/N) > 40$ Td, our μN exceed the Magboltz results by 3%. We note that Magboltz precisely reproduces Nakamura's measurements of the electron drift velocity between 15 and 50 Td [57].

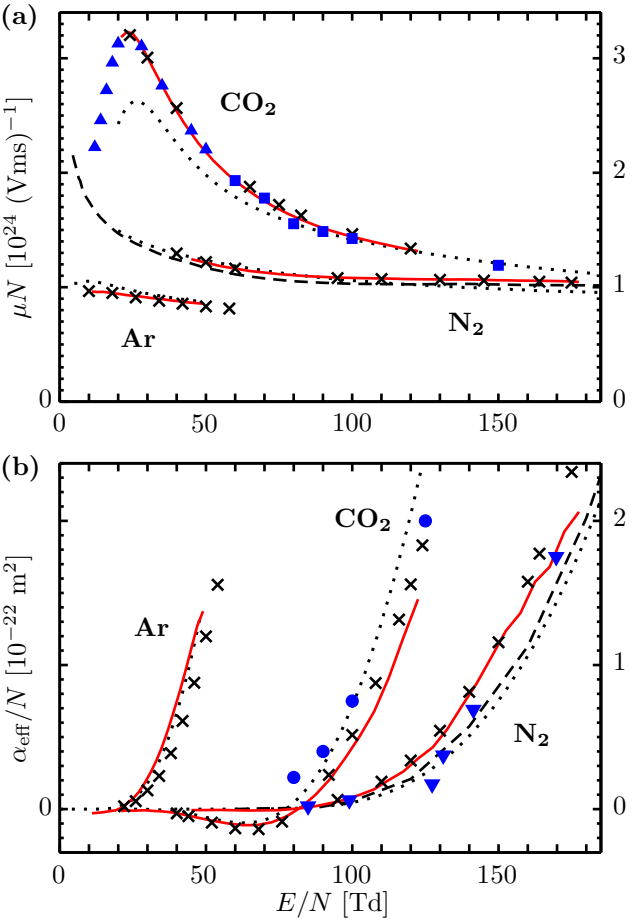

Figure 3.5.: Present results (——) of electron mobility (a), and (b) effective ionization coefficients. Reference data were obtained using Bolsig+ [18] (· · · · · ·), and (×) Magboltz [5]. Experimental reference data in N_2: (– – –) de Urquijo [64], (▼) Haydon [59], and in CO_2: (▲) Elford [58], (■) Raju's recommendations [65], (●) Bhalla [60].

Figure 3.5(b) shows that the $\boldsymbol{\alpha_{\mathrm{eff}}/N}$ from SParX closely agree to the values from Bolsig+. As presented in figure 3.6(a), the $\boldsymbol{N\tau_{\mathrm{D}}}$-results of SParX agree to the longitudinal values from Magboltz.

N_2

For $\boldsymbol{\mu N}$, the difference between our results and Magboltz is $\pm 1\%$. Also Bolsig+ produced values within $\pm 1\%$ of SParX results for $(E/N) < 100$ Td, but for $(E/N) > 100$ Td the present results are up to 10% higher than the values from Bolsig+. The SParX results are in excellent qualitative agreement with de Urquijo's data, but our μN are 5% higher. Perhaps this difference appears because our approach allows for the time required to accelerate and equilibrate the swarm.

The $\boldsymbol{\alpha_{\mathrm{eff}}/N}$ from SParX are nearly the same as the Magboltz values for $(E/N) < 150$ Td. Above 150 Td our results are slightly below the Magboltz results, but reproduce Haydon's value at 165 Td. The SParX data in the range 110 to 180 Td are significantly higher than the values from Bolsig+ and de Urquijo. Between 100 and 150 Td our α_{eff}/N are also higher than Raju's recommendations.

Our $\boldsymbol{N\tau_{\mathrm{D}}}$ above 80 Td correspond to the *transversal* values from Magboltz. Below 80 Td the SParX-results show a tendency towards halfway the transversal and the longitudinal values from Magboltz. Our measured $N\tau_{\mathrm{D}}$ are always higher than the Magboltz results of longitudinal diffusion in the (E/N)-range of the present study.

CO_2

There is a prominent peak of $\boldsymbol{\mu N}$ at 25 Td, which was well resolved by our measurements. Our μN accurately reproduce Elford's measurements between 20 and 50 Td [58]. Again, there is excellent agreement with Magboltz results, only between 50 and 80 Td our values are 3% smaller. In Raju's recommended values, a step of μN is apparent near 70 Td, which was not found in the SParX data.

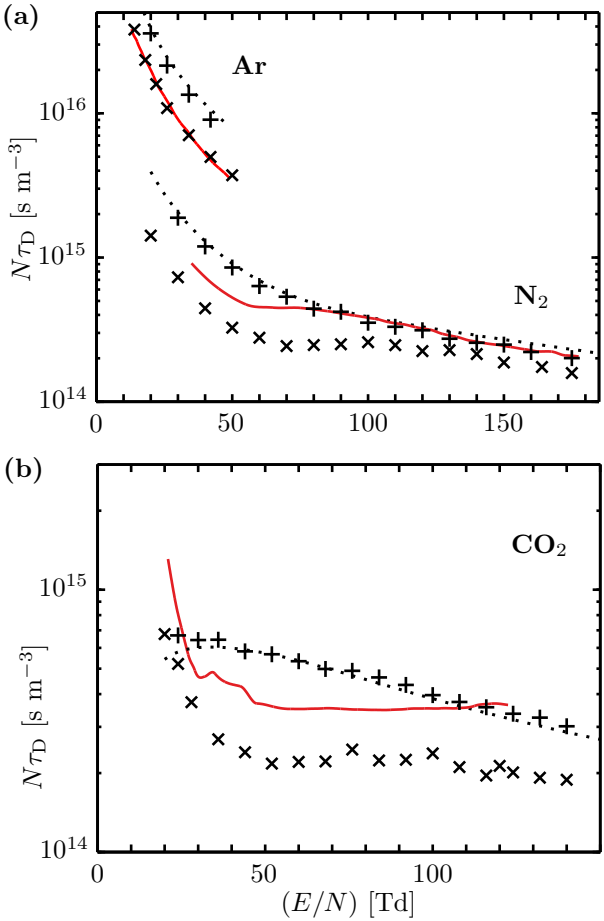

Figure 3.6.: Present results (——) of the diffusion time constant in (a) Ar, N_2, and (b) CO_2. Reference data are Bolsig+ (· · · · · ·), and Magboltz longitudinal (×) and transversal (+) values for selected E/N.

The small negative values $\boldsymbol{\alpha_{\mathrm{eff}}/N}$ for $(E/N) \leq 50$ Td from SParX match to Magboltz results. The two methods also agree on $(E/N)_{\mathrm{crit}}$. However, the minimum of α_{eff}/N from SParX around 65 Td is slightly above the Magboltz value, and for $(E/N) > 100$ Td our results are 5% lower. Raju's recommended values appear much too high between 80 and 100 Td.

The SParX data for $\boldsymbol{N\tau_{\mathrm{D}}}$ and the longitudinal values from Magboltz both show a prominent fall of $N\tau_{\mathrm{D}}$ between 20 and 50 Td, which is not present in the values derived from Bolsig+. However, on the whole (E/N)-range our $N\tau_{\mathrm{D}}$-data are significantly higher than the longitudinal diffusion obtained from Magboltz.

General

The $(\alpha_{\mathrm{eff}}/N)$-data for N_2 and CO_2 shown in figure 3.5(b) seem to make up two groups in each gas. On the one hand, there seems to be agreement between Urquijo's measurements, Bolsig+ and Raju's recommendations, on the other, there is very good agreement between SParX and Magboltz. Moreover, there is no uniform tendency for the difference between the two groups; for N_2, the results of Magboltz and SParX are higher than the other data, but lower for CO_2. Considering the measurements it is obvious that the numerical results and the cross sections on which they are based should be subject of further critical assessment.

It should be remembered that Bolsig+ produces isotropic flux diffusion, that Magboltz produces longitudinal and transversal flux diffusion, and that only longitudinal bulk diffusion is obtained from SParX. From figure 3.6(a) the highly anisotropic diffusion in Ar becomes apparent, with only small differences between longitudinal bulk and flux values, and noticeably higher transversal and isotropic values. These results indicate that anisotropic diffusion is a successful concept for Ar in the (E/N)-range below 50 Td. In this (E/N)-range elastic processes dominate [57]. Whereas for N_2 and CO_2, longitudinal bulk diffusion (SParX data) is substantially larger than the longitudinal flux values produced by Magboltz. From fig-

ure 3.6(b) it becomes apparent that bulk diffusion in CO_2 could be reproduced neither by the Boltzmann solver nor by the Monte Carlo method. Future studies on bulk diffusion in N_2 or CO_2 could also consider effects of inelastic electron-molecule interactions, and a dispersive force due to the space charges.

3.7. Summary and conclusions

The SParX pulsed Townsend (PT) setup was presented, the operation of which is entirely computer controlled. As its components and the processes are robust and reliable, trustworthy experiments can run in an autonomous mode.

3.7.1. Model and analysis method

Current waveforms of PT measurements have been parameterized with the electron transit time T, the ionization rate ν_{eff}, and the diffusion time constant τ_{D}. For any future work on the basis of the PT method, we recommend using these temporal parameters. The previously used spatial parameters required estimating the electron velocity prior to the analysis of measured waveforms. For each of the waveform parameters T, ν_{eff}, τ_{D}, one regression method was presented. These regression methods were applied to our measurements for obtaining the swarm velocity w and the density normalized swarm parameters ν_{eff}/N and $N\tau_{\mathrm{D}}$. Our swarm model and regression methods explicitly take into account non-idealized conditions for electron swarms within the experimental setup, namely effects of electrode misalignment, of laser pulse duration, ion currents, sensor offsets, and the initial lack of swarm equilibrium. It was demonstrated that these regression methods are superior to averaging methods.

3.7.2. Recommendations on Ar, N_2 and CO_2

Electron swarm parameters have been measured in Ar, N_2 and CO_2. Tabulated data of our measurements are provided, which might later be compared to the output of dedicated simulations. The electron mobilities obtained by our method precisely reproduce literature data. It was shown that our electron transport parameters are in good agreement with electron transport parameters from Monte Carlo swarm simulations, except for noticeable differences for ionization rates in Ar, and for diffusion time constants in N_2 and CO_2.

Under the conditions of the present measurements in N_2 and CO_2, the diffusion time constant was increased by strong dispersive effects, which are not included in the Monte Carlo swarm simulation. Such dispersive effects should be mitigated in SParX, e.g. by reducing the space charge density of the swarms. On the other hand, when electron diffusion plays a role for particular applications in molecular gases, such dispersive effects should be included in the model, e.g. by considering experimental data of longitudinal diffusion.

In order to improve the input data for plasma models, one would advise critical assessment and a revision of recommendations for ionization coefficients in N_2 below 170 Td, and for the effective ionization coefficients in CO_2 below 120 Td.

4. Response analysis of electron attachment rates to C_3F_8 and SF_6 in buffer gases

This chapter is based on a published article [66].

4.1. Introduction

One can investigate the attachment parameters of a sample molecule by means of swarm parameter measurements in buffer gases [67–69], when the relative concentration (mixing ratio) k of the sample molecule is small. In buffer gases with well known electron energy distribution (EEDF), like Ar, N_2 or CO_2, such experimental results are important for assessing the attachment cross sections of a sample molecule [67, 69, 70].

The results of swarm experiments in gas mixtures can be applied more generally and readily, when the experimental technique achieves a separation between the swarm parameters of the buffer gas and the effects of the sample gas. For example, the swarm data of gas mixtures were evaluated for the rate constants of electron attachment to a sample molecule [67, 71]. However, these analyses were limited to such values of E/N where ionization could be neglected. We aim for applying a similar technique also near the critical field strength $(E/N)_{\mathrm{crit}}$, where the ionization rate equals the attachment rate, because this (E/N)-range is of particular interest for high voltage insulation technology.

For certain mixtures of an electronegative gas and a buffer gas, and for particular values of E/N, a linear relation appears between

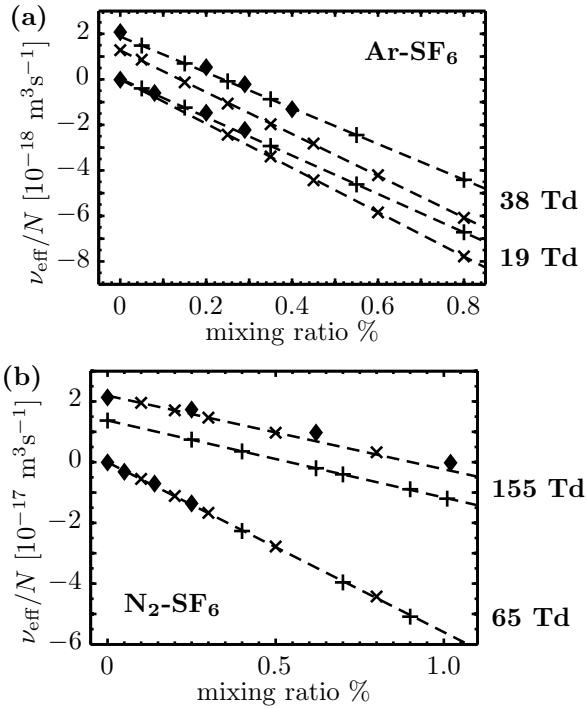

Figure 4.1.: Measurements (♦) of the effective ionization rate constant, and the values (+) calculated by a Boltzmann solver [18] or (×) simulated by a Monte Carlo method [5] as a function of the mixing ratio of (a) SF_6 in Ar, and (b) SF_6 in N_2. The lines (– – –) represent the linear trends of simulated or calculated values.

k and the effective ionization rate constant ν_{eff}/N. This is shown, for example, in figure 5 of [72] and figure 8 of [73]. Such a linear relation also appears in our measurements and in the results of two mutually independent numerical methods [5, 18], as one can note from the figures 4.1 and 4.6 of this chapter.

Based on the assumption of a linear relation between ν_{eff}/N and k, we attempt to develop a linear response technique as a more convenient method for investigating the electron attachment parameters of sample molecules. This technique shall be tested with SF_6 which is a gas with well known parameter values [74]. SF_6 can therefore be considered as providing a benchmark [2, 14]. We compare our measurements to numerical results because experimental data are scarce in the parameter range of the present study [72, 73]. Subsequently, the linear response technique is applied for testing the attachment cross sections of octafluoropropane (C_3F_8).

4.1.1. Octafluoropropane

Previous work on C_3F_8 has been reviewed in [75, 76]. More recently, a new set of electron collision cross sections was derived from drift tube measurements [77], and the electron-impact dissociation cross sections were remeasured [78]. It is known that the electron attachment rate constant depends on the total gas density and the gas temperature. For 300 K and high total gas density, $\sim 10^{26}$ m^{-3}, the transient anion can be stabilized due to 3-body processes, and the non-dissociative attachment rate is comparable to the dissociative attachment rate. For temperatures > 500 K, only dissociative attachment was observed [79]. In consequence, a dissociative attachment cross section for 300 K was derived by extrapolating results obtained at elevated temperature. The present study is made at intermediate gas densities, $\sim 10^{24}$ m^{-3}, at 300 K, where our methods are not sensitive enough to detect a minor influence of density dependent processes. We argue that an independent test of the attachment cross sections is possible with the data of the present study.

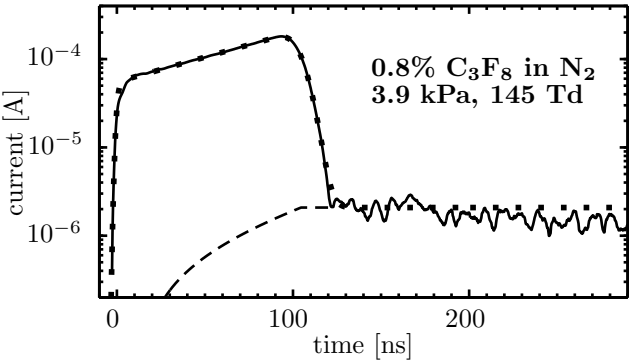

Figure 4.2.: Logarithmic plot of measured swarm drift current (——) and a fit (· · · · · ·) of the presently used swarm current model which includes the ion current (– – –). The electrode spacing was $d = 15$ mm.

4.2. Methods of linear response analysis

A pulsed Townsend (PT) electrical method is used. The experimental setup, its operation and the signal processing techniques have been described in chapter 3.

4.2.1. Linear response technique

The effective ionization rate constant of a gas mixture $(\nu_{\mathrm{eff}}/N)_{\mathrm{k}}$ with mixing ratio k is defined by the EEDF $F(\varepsilon)_{\mathrm{k}}$ and by the ionization and attachment cross sections of the sample gas, $\sigma_{\mathrm{i}}(\varepsilon)$ and $\sigma_{\mathrm{a}}(\varepsilon)$ respectively, and the ionization minus the attachment cross sections of the buffer gas $\sigma_{\mathrm{B}}(\varepsilon)$, see also (10) in [18].

$$(\nu_{\mathrm{eff}}/N)_{\mathrm{k}} = \sqrt{\frac{2}{m_{\mathrm{e}}}} \int_0^\infty \varepsilon \left\{(1-k)\,\sigma_{\mathrm{B}} + k\,(\sigma_{\mathrm{i}} - \sigma_{\mathrm{a}})\right\} F_{\mathrm{k}} \mathrm{d}\varepsilon \ , \quad (4.1)$$

where m_e is the electron mass and

$$\int_0^\infty \sqrt{\varepsilon} F_k \mathrm{d}\varepsilon = 1 \, .$$

We assume that $F_k(\varepsilon)$ is very similar to the EEDF of the pure buffer gas $F_B(\varepsilon)$:

$$F_k \to F_B \, \text{for small} \, k \, . \tag{4.2}$$

Then (4.1) resolves to

$$\begin{aligned}(\nu_{\text{eff}}/N)_k \approx & (\nu_{\text{eff}}/N)_B \\ & - k\sqrt{\frac{2}{m_e}} \int_0^\infty \varepsilon \left\{\sigma_B - \sigma_i + \sigma_a\right\} F_B \mathrm{d}\varepsilon \end{aligned} \tag{4.3}$$

$$(\nu_{\text{eff}}/N)_k \approx (\nu_{\text{eff}}/N)_B - k\, r_{BA} \, , \tag{4.4}$$

with the effective ionization rate constant of the pure buffer gas $(\nu_{\text{eff}}/N)_B$, and the linear response parameter r_{BA}, which constitutes a characteristic property of a particular combination of a buffer gas B and a sample gas A.

Equation (4.4) evaluates the sensitivity of ν_{eff}/N on changes of k. It shall be used for obtaining r_{BA} as a function of E/N from calculated, simulated or measured ν_{eff}/N. One expects $r_{BA} > 0$ for the sample gases and the E/N-range of the present study because the term σ_a predominates in the convolution integral (4.3).

Conditions for valid application

Assumption (4.2) holds only if the sample gas does not perturb the momentum and energy balance of the electron swarm [70, 80]. Only then it is valid to apply (4.3) for an interpretation of the linear response parameters. Otherwise, a perturbation of F_B must be taken into account when making a connection between $r_{BA}(E/N)$ and $\sigma_a(\varepsilon)$.

The influence of electron attachment on F_B can be neglected only if the attachment rate ν_a is much smaller than the total energy transfer rate [80]

$$\nu_a \ll \frac{2m_e}{M}\,\nu_m + \sum_j \delta_j \nu_j \,, \tag{4.5}$$

where M is the effective mass of the gas constituents, ν_m is the momentum transfer collision rate, and ν_j are the rates of inelastic processes with fractional energy loss δ_j.

In particular gas mixtures, condition (4.5) may be violated, and electron attachment to the sample gas can strongly affect F_B even for small k. For example, such perturbations of F_B were previously found at $(E/N) \leq 20$ Td with 0.5% F_2 in Ar [81], or with 0.1% NF_3 in Ar [82]. For every particular combination of gases B-A, it is therefore necessary to test the range of E/N and k where a linear relation (4.4) can appear (see also sections 4.4 and 4.5).

4.2.2. Numerical methods and cross sections

For *simulating* electron transport parameters, we use a Monte Carlo (MC) method (Magboltz [5] version 9.0.1). The simulation settings were: 4×10^8 real collisions, total gas pressure 75 torr and temperature 297 K. Magboltz uses Itoh's cross section set for SF_6 [83], and proprietary sets for Ar, N_2, CO_2 and C_3F_8. We note that the proprietary dissociative attachment cross section of C_3F_8 closely corresponds to $0.85\times$ the recommended cross section [75].

For *calculating* electron transport data, we use a solver (Bolsig+ [18] version 11.2011) for the 2-term expanded Boltzmann equation (BE) with a cross section database (SIGLO [84] version 11.2011). It includes Phelps' cross section sets for Ar and N_2 tested in [18], Morgan's set for CO_2, and Phelps' set for SF_6 [85]. The solver settings were: Precision 10^{-13}, Convergence 10^{-5}, Iterations 100, gas temperature 297 K, temporal growth model, equal energy sharing after ionization.

There are well known limitations of using 2-term BE methods for testing cross sections [69]. However, in the (E/N)-range under study, we argue that the 2-term BE method yields rate constants with satisfactory precision, provided that an accurate cross section set is available. It must be emphasized that the BE and MC methods are entirely different, and that their results are mutually independent because they are based on different cross section sets. Our choice of numerical methods and cross sections was made in order to provide disparate reference data for SF_6-mixtures.

4.3. Results

This chapter concerns binary mixtures of one sample gas, SF_6 or C_3F_8, and one buffer gas, Ar, N_2 or CO_2. The purity of the gases, and the mixing ratios under investigation are summarized in table 4.1. Table 4.2 specifies the ranges of total gas pressure for the measurements. The present analysis also uses swarm parameters of the pure buffer gases given in the previous chapter.

4.3.1. Mixture preparation

Gas mixtures were prepared directly in the experimental vacuum vessel which has a base pressure $< 10^{-5}$ Pa. After the vessel had been vented with the buffer gas B, the sample gas A was filled with the desired partial pressure. Then B was added to reach the desired total pressure. Gas pressure and temperature were continuously measured, and the total gas density N was determined at any time with uncertainty $\pm 1\%$ in the relevant pressure range 50 Pa to 11 kPa. Gas mixtures with $k < 0.5\%$ have been prepared starting from a mixture with $k = 0.5\%$ by pumping out part of the mixture and then refilling B to the desired total pressure.

Table 4.1.: Mixing ratios of the sample gases, and the measured critical field strength of the gas mixtures. The gas purity is stated in brackets ($3.0 \equiv 99.9\%$). * Tabulated swarm parameter results given in the appendix.

	SF_6 (3.0)		C_3F_8 (4.0)	
buffer gas	mixing ratio %	$(E/N)_{\mathrm{crit}}$ (Td)	mixing ratio %	$(E/N)_{\mathrm{crit}}$ (Td)
Ar (6.0)	0.08	30.5	0.17	25.3
	0.20*	37.5	0.25	32.7
	0.29	41.0	0.51*	34.2
	0.40	43.5	1.01	40.2
N_2 (5.0)	0.05		0.09	79.0
	0.14		0.37	93.8
	0.25*	129	0.81*	104
	0.62	144	1.51	113
	1.02	153		
CO_2 (5.0)			0.18	83.9
			0.27	85.1
			0.81*	92.5
			1.21	95.8

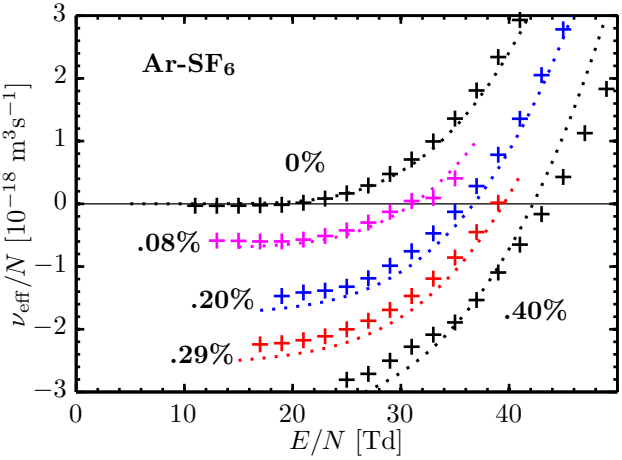

Figure 4.3.: Measured (+) and BE-calculated (· · · · · ·) effective ionization rate constants ν_{eff}/N in Ar/SF_6 for various mixing ratios.

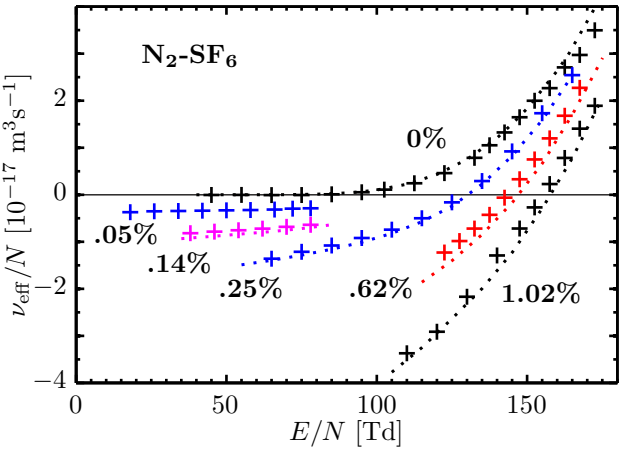

Figure 4.4.: Measured (+) and MC-simulated (· · · · · ·) effective ionization rate constants ν_{eff}/N in N_2/SF_6 for various mixing ratios.

Table 4.2.: Overview of the parameter range of measurements, and a catalogue of the numbers of figures and tables where the results are presented. Refer to section 4.3.3 for column descriptions.

		ν_{eff}/N		r_{BA}		
buffer and sample gas	pressure (kPa)	overview (figure)	linearity (figure)	(E/N)-range (Td)	$\langle\varepsilon\rangle$-range (eV)	plot (figure)
Ar/SF_6	$2-8$	4.3	4.1(a)	$19-43$	$5.51-6.00$	4.5
N_2/SF_6	$2-8$	4.4	4.1(b)	$40-165$	$1.11-4.27$	4.5
Ar/C_3F_8	$2-8$		4.6(a)	$22-46$	$5.61-6.06$	4.8
N_2/C_3F_8	$2-10.5$		4.6(b)	$20-150$	$1.03-3.85$	4.8
CO_2/C_3F_8	$2-9$		4.6(c)	$28-116$	$1.07-4.45$	4.8

4.3.2. Measurement parameters and procedures

The swarm parameter measurements were made at room temperature 293 to 300 K. After one measurement sequence had been completed, the total pressure was reduced by pumping, and a subsequent measurement sequence was carried out. In this way the same gas mixture was investigated for 4 to 6 different N-values. The PT waveforms have been recorded for electrode spacings $d = (17, 15, 13, 11)$ mm in the E/N-range of interest. The cumulative uncertainty of the (E/N)-values was $\pm 1.5\%$.

In the parameter range of the present study, the measured waveforms and the modelled swarm currents almost coincide. Figure 4.2 shows an excellent agreement between the measured and calculated currents. The PT waveforms have been evaluated for the swarm parameters ν_{eff}/N and w. From the (ν_{eff}/N)-data, the critical field strength $(E/N)_{\text{crit}}$ was determined by interpolation. The (ν_{eff}/N)-data of a pair of gases B-A with different k were plotted for selected values of E/N, as it is shown for example in figures 4.1 and 4.6. After we had checked the validity of a linear relation between ν_{eff}/N and k, we applied (4.4) in order to obtain r_{BA}.

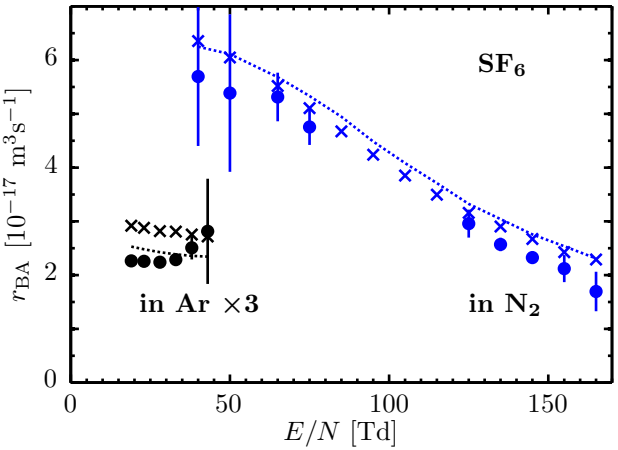

Figure 4.5.: Measured (• with error |), MC-simulated (×) and BE-calculated (· · · · · ·) linear response r_{BA} of ν_{eff}/N on adding 1% SF_6 into Ar or N_2. The data for Ar/SF_6 were multiplied by 3.

4.3.3. Data presentation

In table 4.2 the measurement parameters are specified for a gas mixture B-A, and the corresponding results are attributed.

Effective ionization rate constant ν_{eff}/N

The (ν_{eff}/N)-results are classified by two columns of table 4.2. These columns denote

1. a figure number where our measurements of ν_{eff}/N are presented together with reference data.

2. a figure number where ν_{eff}/N was plotted as a function of k for selected values of E/N.

Linear response parameters r_{BA}

The r_{BA}-results are classified by three columns of table 4.2. These columns denote

1. a range of E/N where r_{BA} was derived,
2. and the corresponding range of mean electron energies $\langle\varepsilon\rangle$ obtained with the MC simulation for the buffer gas.
3. a figure number where r_{BA} was plotted as a function of E/N.

The r_{BA}-results have been normalized to $k = 1\%$. The 95% confidence interval of r_{BA} is given as the error of the experimental data. The experimental results of $r_{\mathrm{N2/C3F8}}$ and $r_{\mathrm{CO2/C3F8}}$ are listed in table A.12.

Supplemental results

- The experimental values of $(E/N)_{\mathrm{crit}}$ are listed in table 4.1.
- For N_2/C_3F_8, selected experimental results of the reduced electron mobility $\mu N = wN/E$ are presented in figure 4.7.
- For selected mixtures, as indicated in table 4.1, the tabulated swarm parameters are given in the appendix.

4.4. Benchmark with SF_6

Applicability of the method

In Ar/SF_6 mixtures, assumption (4.2) may be violated because $\sigma_{\mathrm{a}}(\varepsilon \to 0\,\mathrm{eV})$ is very large, and because the grand total cross section $\sigma_{\mathrm{tot}}(\varepsilon \approx 0.2\,\mathrm{eV})$ is relatively small due to the Ramsauer minimum of Ar. In N_2/SF_6 mixtures, assumption (4.2) may be violated for values of ε below the threshold of vibrational inelastic collisions with N_2. We argue that a perturbation of F_{B} only weakly affects ν_{a} in

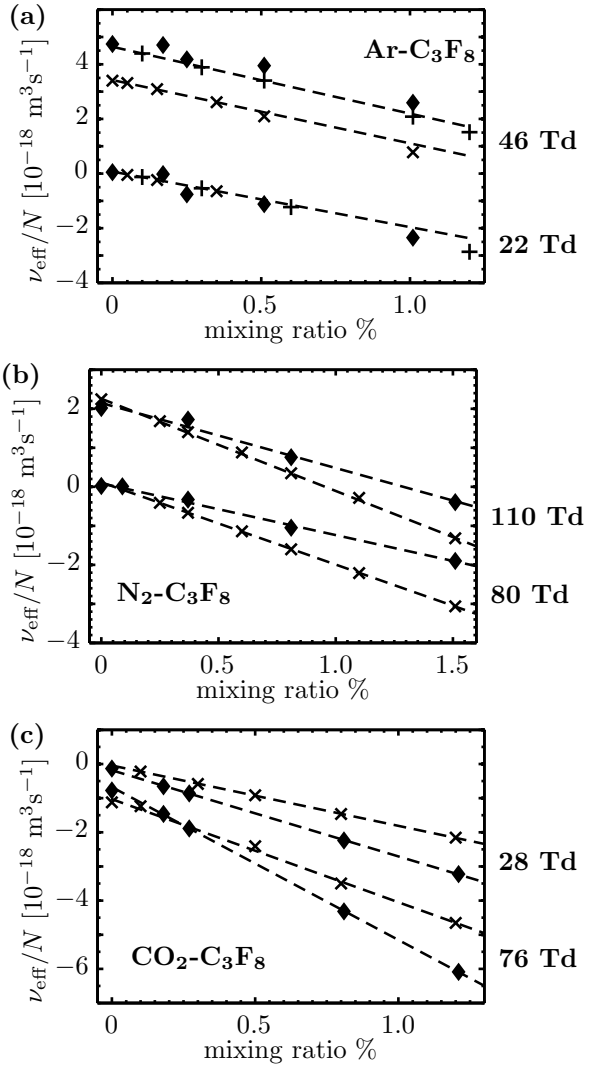

Figure 4.6.: Measured (♦), BE-calculated (+) and MC-simulated (×) effective ionization rate constants in mixtures of (a) Ar/C_3F_8, (b) N_2/C_3F_8, and (c) CO_2/C_3F_8. The lines (– – –) represent linear trends.

the parameter range of the present study, because the mean electron energy $\langle\varepsilon\rangle$ is sufficiently high, and condition (4.5) is met. The linear response method (4.4) may be applied in the (E/N)-range of the present measurements. A linear relation between ν_{eff}/N and k is clearly observable in figure 4.1.

Assessment of results

At low E/N, e.g. 65 Td in N_2/SF_6 or 19 Td in Ar/SF_6, both numerical methods give results consistent with measured values, as it is apparent from figure 4.1. However, at higher E/N the (ν_{eff}/N)-results from BE and MC are significantly different from each other, probably because they employ somewhat different sets of cross sections. In the case of Ar/SF_6, our measurements agree fairly well with the BE-results, see also figure 4.3. In the case of N_2/SF_6, the measurements closely correspond to the MC-results, see also figure 4.4.

As one can see from figure 4.5, the BE- and MC-results nearly coincide on the values of $r_{\text{N2/SF6}}$. The experimental data seem to be $\sim$5% smaller, but they qualitatively reproduce the BE- and MC-values. In the case of Ar/SF_6, the experimental results seem to be slightly smaller than the results of both numerical methods. We note that the cross section for the formation of SF_5^- was found to be much smaller than the ones used in the present calculations and simulations [14]. It might be necessary to adopt the cross sections from [14] in order to resolve the present small discrepancy between measurements and numerical results.

The response analysis of experimental (ν_{eff}/N)-data (figure 4.5) yielded relatively small errors when the analysis was based on at least four data points. Large uncertainties of r_{BA} appeared where the response analysis was based on three data points only, i.e. for 40 and 50 Td in N_2/SF_6, or for 43 Td in Ar/SF_6. These r_{BA}-values with large uncertainties also seem to be qualitatively inconsistent with the reference values. It looks like the precision of experimental r_{BA}-data is adequately represented by stating the 95%-confidence

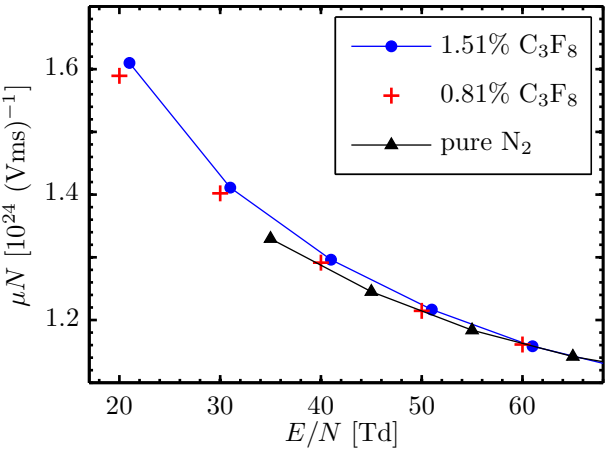

Figure 4.7.: Pulsed Townsend results of the reduced electron mobility in N_2/C_3F_8 mixtures. The lines are merely for guiding the eye.

interval of the linear response parameter.

4.5. Test of the C_3F_8 attachment cross section

Applicability of the method

Figure 2 of [67] and figure 1 of [79] indicate a non-linear relation between k and the electron attachment rate constant ν_a/N_A, with N_A corresponding to the partial number density of C_3F_8. It should be noted that these values ν_a/N_A had been derived from measurements of the attachment coefficient η, using

$$\nu_a/N_A = \frac{\eta w_B}{N_A} , \tag{4.6}$$

where w_B is the electron drift velocity of the buffer gas.

It is apparent from figure 2 of [77] and from figure 4.7 of the present chapter that w significantly increases for $(E/N) < 40$ Td,

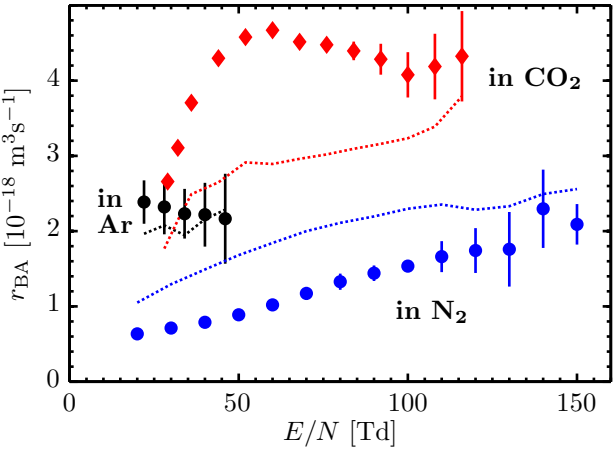

Figure 4.8.: Measured (symbols with error |) and MC-simulated (·····) linear response r_{BA} of ν_{eff}/N on adding 1% **C_3F_8** into Ar (●), N_2 (●) or CO_2 (♦).

when C_3F_8 is added into N_2 or Ar. We argue that the relation between η and k is non-linear because of the change of w with k.

In contrast, we measured ν_{eff}/N and found a linear relation between ν_{eff}/N and k for $k \leq 1.5\%$ in N_2, as one can note from figure 4.6(b). An application of the linear response method (4.4) seems to be permitted for the analysis of N_2/C_3F_8. In Ar buffer gas, see figure 4.6(a), the (ν_{eff}/N)-values for $k \approx 1\%$ seem to deviate from a linear trend. In consequence, the linear response analysis of Ar/C_3F_8 was restricted to $k \leq 0.51\%$.

In the case of CO_2/C_3F_8, assumption (4.2) seems to hold because both species have vibrational excitation cross sections with relatively low threshold energy. Then it is valid to apply (4.4).

Assessment of results

As shown in figure 4.8, our results for $r_{Ar/C3F8}$ and the values from the MC simulation agree within the experimental uncertainty. The

agreement indicates a suitable scaling of the total area of σ_a. The linear responses derived from the MC simulation for the N_2 or CO_2 buffer gases, however, are not consistent with the present experimental data. The experimental $r_{N2/C3F8}$ are much *smaller* than the MC values. On the other hand, the experimental $r_{CO2/C3F8}$ are much *larger* than the MC values.

In figure 4.8 the experimental data show a strong increase of $r_{CO2/C3F8}$ between 30 and 50 Td. A maximum of $r_{CO2/C3F8}$ appears near 60 Td. It is not present in the MC results. A monotonic increase of $r_{N2/C3F8}$ with increasing E/N consistently appears in the experimental and simulated results. The uncertainty of the experimental response data is particularly large in such (E/N)-ranges where strong ionization occurs. In these (E/N)-ranges the experimental errors of k or E/N can strongly influence the measurement of ν_{eff}. In consequence, a relatively large scatter can appear in the corresponding (ν_{eff}/N)-values. The scatter causes a large 95%-confidence interval of r_{BA}. For $(E/N) < 100$ Td, the precision of the experimental response data should be sufficient for testing revised attachment cross sections of C_3F_8.

4.6. Summary and conclusions

Electron swarm methods have been successfully applied for investigating the effects of small amounts of a strongly electronegative sample gas in a buffer gas. We evaluated the sensitivity of the effective ionization rate constant to changes of the mixing ratio. The analysis yielded the linear response parameters as a function of the reduced electric field strength.

Our evaluation technique was benchmarked with an analysis of the effective ionization rate constants of SF_6-mixtures. The benchmark involved the results of our own pulsed Townsend measurements, the results of a well-approved Monte Carlo swarm method, and the results of a standard solver for the two-term expanded Boltzmann equation. We found satisfactory agreement between the linear re-

sponse parameters derived from the results of the three different methods.

We gave directions for an interpretation of the linear response parameters with respect to the influence of the sample gas on the electron energy distribution in the buffer gas. A connection was made between the linear response parameters and the attachment cross sections of a sample molecule.

The linear response technique was applied for testing the attachment cross section of C_3F_8. For Ar, N_2 and CO_2 buffer gases, the linear response was simulated using a Monte Carlo swarm method with the recommended attachment cross sections. Experimental response data have been determined from our own pulsed Townsend measurements. As far as we know, the present work is the first report on swarm parameter measurements in CO_2-C_3F_8 mixtures. For the admixtures of C_3F_8 to Ar or N_2, our measurements of the effective ionization rate constant complement the data hitherto in the literature by expanding the range of mean electron energies covered.

The incompatibility of Monte Carlo simulations of electron attachment to C_3F_8 in N_2 or CO_2 with the experimental data indicate the necessity to re-assess the attachment cross sections of C_3F_8.

5. Electron attachment to c-C_4F_8O from swarm measurements in buffer gases

This chapter is the basis for a manuscript submitted to *The European Physical Journal D, POSMOL special issue.*

5.1. Introduction

Octafluorotetrahydrofuran (c-C_4F_8O) recently became commercially available with the designated application as cleaning agent for chemical vapour deposition chambers. c-C_4F_8O was considered for substituting widely used plasma processing gases with high global warming potential [3]. It has been demonstrated that c-C_4F_8O can replace C_4F_{10} as radiating medium in Cherenkov detectors [6]. No reports of electron transport coefficients or electron collision cross sections of c-C_4F_8O are known to the authors.

Gas mixtures containing ketones are considered as SF_6 substitutes [86–88] for high voltage insulation applications. We study c-C_4F_8O as an example for such application scenarios, because the physical properties of c-C_4F_8O and the ketones are similar enough, and it is more comprehensively covered than the ketones in the relevant literature. It has a boiling point $T_b = -0.8$ °C, and vapour pressure ∼200 kPa at 20 °C. On the other hand, high voltage technical equipment is being operated at ∼600 kPa gas pressure at ambient temperatures down to about −30 °C. In such operating conditions, c-C_4F_8O can only be used with low mixing ratio in a buffer gas.

For the present investigation, we measured the electron swarm parameters of c-C_4F_8O with mixing ratios $\leq 1.2\%$ in binary mixtures with Ar, N_2 or CO_2. Our results of the effective ionization rates were further evaluated, using the linear response technique [66]. Finally, it is attempted to estimate attachment cross sections consistent with our experimental results of electron attachment rates.

5.2. Swarm results and linear response analysis

The experimental procedures and evaluation techniques applied in the present study have been comprehensively described in previous chapters. The sample gas c-C_4F_8O has been obtained from Linde with a quoted purity $2.5 \equiv 99.5\%$. Table 5.1 summarizes the investigated gas mixtures.

5.2.1. Swarm parameters

The swarm parameter measurements were made at room temperature 293 to 300 K, with the experimental settings specified in table 5.1. With these experimental parameters, the electron swarm model, which is the basis for obtaining the swarm parameters, was fully consistent with the measured waveforms, as one can see from figure 5.1(a). The waveform analysis yielded the swarm drift velocity w, the effective ionization rate constant ν_{eff}/N, and the density normalized diffusion time constant $N\tau_{\text{D}}$. With other experimental settings, see for example figure 5.1(b), processes may occurr which are not included in the model. In those cases the waveforms have been removed from the analyses.

Figure 5.2 presents the (ν_{eff}/N)-results in Ar/c-C_4F_8O mixtures. For selected gas mixtures, as indicated in table 5.1, the swarm parameters are listed in the appendix in tables A.4, A.8 and A.11. The experimental uncertainty was $\pm 1.5\%$ for E/N. The statistical uncertainty was $\pm 0.5\%$ for w, $\pm 2\%$ for $N\tau_{\text{D}}$, and for ν_{eff}/N it is given in the result tables (A.4, A.8, A.11).

Table 5.1.: Investigated mixing ratios of c-C_4F_8O in buffer gases (gas purity in brackets), and the measured critical field strength ±1.5% uncertainty. The experimental conditions are specified by stating the ranges of total gas pressure, of E/N, and of the electrode spacing. * Tabulated swarm parameter results given in the appendix.

buffer gas	experimental conditions	mixing ratio %	$(E/N)_{\mathrm{crit}}$ (Td)
Ar	2 - 8 kPa	0.21*	30.0
(6.0)	24 - 54 Td	0.40	32.6
	11 - 17 mm	0.60	36.7
		1.01	41.0
N_2	2 - 4 kPa	0.15	104
(5.0)	20 - 130 Td	0.20	109
	11 - 17 mm	0.30	113
		0.40*	119
		0.60	121
CO_2	2 - 4 kPa	0.15	86.0
(5.0)	20 - 116 Td	0.30	90.5
	11 - 17 mm	0.40	92.5
		0.60	97.2
		0.81*	100
		0.99	102
		1.21	106

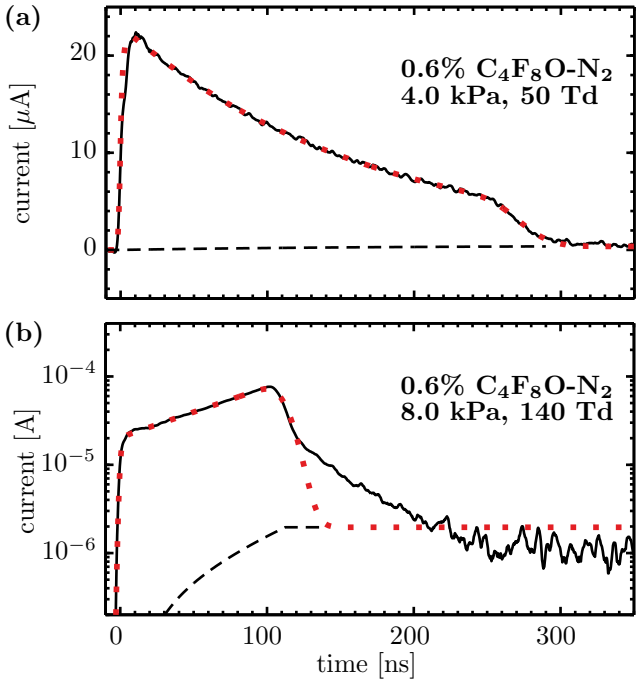

Figure 5.1.: Measured swarm drift currents (——), and their analytical approximation (· · · · · ·) including ion currents (– – –) for 0.6% c-C_4F_8O in N_2. Panel (a) shows excellent agreement between a waveform and the approximation derived from the usual swarm model [41], and (b) shows a discrepancy between measured and modelled currents for $t > 120$ ns. Thus, it was not feasible to evaluate waveform (b).

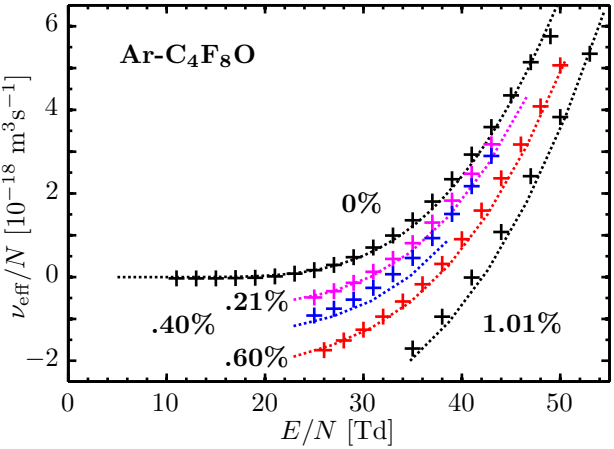

Figure 5.2.: Measured (+) effective ionization rate constants in various Ar/c-C_4F_8O mixtures, and the values (· · · · · ·) calculated using preliminary cross sections (see section 5.3).

From the (ν_{eff}/N)-data, the critical field strength $(E/N)_{\text{crit}}$ was determined where the (ν_{eff}/N)-value equals zero. The results of $(E/N)_{\text{crit}}$ are given in table 5.1.

5.2.2. Response analysis

For selected values of E/N, the measured ν_{eff}/N were plotted as a function of the mixing ratio k. As one can note from figure 5.3, a linear relation was apparent between ν_{eff}/N and k for $k \leq 0.6\%$ in Ar, for $k \leq 0.4\%$ in N_2, and for $k \leq 1.0\%$ in CO_2. For these small k, it is appropriate to apply the linear response technique [66].

The response analysis was based on

$$(\nu_{\text{eff}}/N)(k) = (\nu_{\text{eff}}/N)_{\text{B}} - rk \,, \tag{5.1}$$

where the constant term $(\nu_{\text{eff}}/N)_{\text{B}}$ represents the effective ionization rate constant of the buffer gas. The linear term r describes the change of ν_{eff}/N due to adding the sample gas. Note that definition

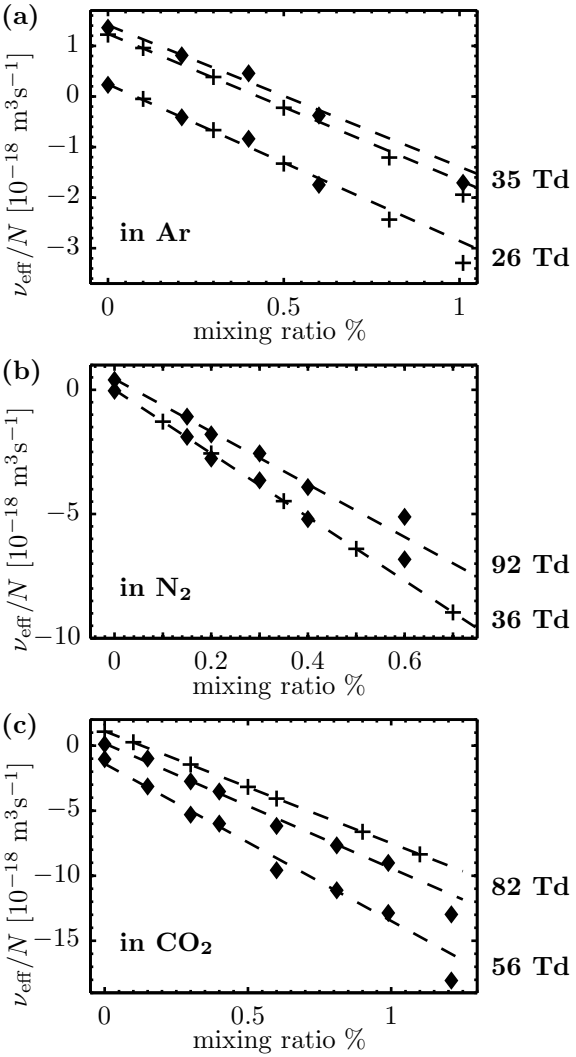

Figure 5.3.: Measured (♦) effective ionization rate constants at selected values of E/N for various mixtures containing c-C_4F_8O, and the values (+) calculated using preliminary cross sections (see section 5.3). The lines (– – –) represent linear trends.

(5.1) leads to positive r for strongly attaching sample gases.

The response results are presented in figure 5.4, and table A.13 gives r for N_2 and CO_2 buffer gases. In these cases the errorbars correspond to the 95% confidence interval of the linear regression parameter.

5.3. Estimation of c-C_4F_8O attachment cross sections

There are well known procedures for extracting cross sections from swarm parameters [69,70]. Such deconvolution procedures have been adopted for obtaining preliminary attachment cross sections σ_a of c-C_4F_8O from our swarm data.

1. Assume an arbitrary σ_a.
2. Calculate the corresponding linear responses r_{test} for the 3 buffer gases, using a solver for the two-term expanded Boltzmann equation [18].
3. Compare r_{test} with the experimental r.
4. Vary σ_a until r_{test} and r agree within experimental uncertainty.

5.3.1. Representation of cross sections

The Boltzmann solver and the cross sections of the buffer gases are defined and discussed in section 4.2.2.

As there is no previous data available on c-C_4F_8O, a fully arbitrary cross section set was constructed.

For practical reasons, the attachment cross sections σ_a are represented by ellipses in the σ-ε-space, which are specified by setting a center value ε_c on the electron energy axis, and the length of two semi-axes a and b, respectively. It was necessary to assume two ellipses, σ_{a1} and σ_{a2}, because a representation with only one ellipse always lead to significant discrepancies between r_{test} and r.

Table 5.2.: Ellipse parameters of the preliminary attachment cross sections σ_{a1} and σ_{a2}: The ranges of values covered during the deconvolution procedure are given, and their values for the best match with experimental data.

	center	semi-axes	
	ε_c (eV)	a (10^{-21} m^2)	b (eV)
range	$0-4$	$0-9$	$0.3-1.2$
σ_{a1}	0.32	4.0	0.6
σ_{a2}	1.9	3.2	0.7

An ionization potential of 11.6 to 12.5 eV was calculated previously, using density functional theory [89]. As an ionization cross section, we adopt the shape and magnitude of the C_3F_8 ionization cross section [75], and assume a threshold energy of 12 eV.

The elastic and excitation processes were approximated with the corresponding cross sections of C_3F_8 [75], using the tabulated values from Magboltz (see also section 4.2.2).

Certainly, these cross sections are not a physically accurate representation of the molecule. They can be usefully applied only under certain conditions. For highly diluted c-C_4F_8O in buffer gases, ν_{eff}/N can be calculated, because the elastic, excitation and ionization collisions with c-C_4F_8O can be regarded as minor disturbances which do not require accurate representation. It must be emphasized that σ_a strongly influences the calculated ν_{eff}/N and r_{test} in the parameter range of the present study, and therefore quantitative properties of σ_a could be extracted from the measurements.

5.3.2. Deconvolution of swarm data

The 3 parameters of σ_{a1} and σ_{a2}, in total 6 degrees of freedom, were varied within the limits specified in table 5.2. The remaining cross sections were kept constant.

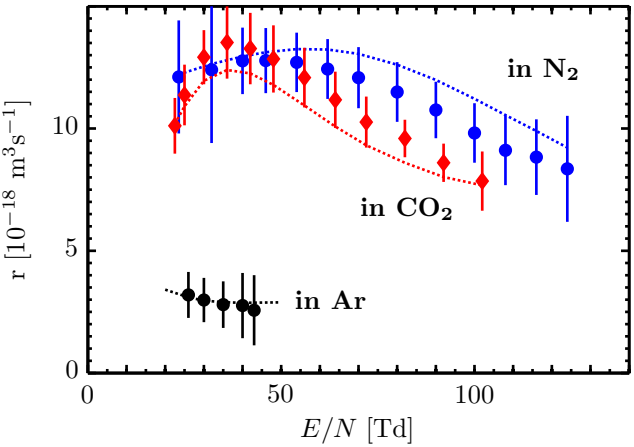

Figure 5.4.: Change of effective ionization rate constants on adding 1% c-C_4F_8O to Ar (•), N_2 (•), or CO_2 (♦).

The best match between r_{test} and r was obtained with the ellipse parameters given in table 5.2. Using these σ_{a1} and σ_{a2}, the values ν_{eff}/N have been calculated and plotted in figures 5.2 and 5.3. The corresponding r_{test} are shown in figure 5.4. Figure 5.5 presents these σ_{a1} and σ_{a2} in comparison to physically realistic attachment cross sections of selected molecules.

5.4. Discussion

5.4.1. Electron attachment to c-C_4F_8O

One can note from figure 5.4 that the electron attachment rates are relatively small for $(E/N) < 30$ Td in N_2 and CO_2. The largest r were observed around 40 Td. These findings indicate that $\sigma_{\text{a}}(\varepsilon)$ is small for electron energy $\varepsilon \to 0$ eV. Indeed, as shown in figure 5.5, the preliminary σ_{a1} is much smaller than the attachment cross sections of c-C_4F_8, or e.g. SF_6, for low ε. It is evident that c-C_4F_8O has relatively large σ_{a} for electrons with ε of a few eV. The corre-

sponding resonant dissociative attachment processes are tentatively represented by σ_{a2}.

In general, the calculations based on the preliminary σ_a are consistent with r within the experimental uncertainty. The maximum of r_{CO2} was reproduced qualitatively. For $(E/N) > 60$ Td, the calculations reproduced the upper error limit of experimental r_{N2}, and the lower one of r_{CO2}.

5.4.2. Effects in N_2 buffer gas

A current waveform, see figure 5.1(b), was recorded with a choice of experimental parameters outside of the range specified in table 5.1: Larger $E/N = 140$ Td, and higher total pressure 8 kPa. Under these conditions the photocathode was coated by a dusty white layer, which probably consists of c-C_4F_8O dissociation products. It looks like the occurrence of swarm electrons with high ε led to large dissociation rates of c-C_4F_8O.

Figure 5.1(b) shows the observation of substantial currents after the swarm bulk has traversed the electrode gap. Such currents can arise from a delayed production of electrons, probably due to Penning ionization or electron detachment [90, 91].

5.5. Conclusions and Outlook

Electron attachment parameters of c-C_4F_8O as a function of E/N have been obtained from measured swarm parameters, using the linear response technique.

It is evident that c-C_4F_8O has relatively large attachment cross sections. Qualitatively, the results show that attachment of low energy electrons plays a minor role compared to the attachment of electrons with energies of a few eV.

Preliminary attachment cross sections have been estimated, which are consistent with the present experimental results of attachment rates in mixtures with Ar, N_2 and CO_2. Certainly, the shapes of

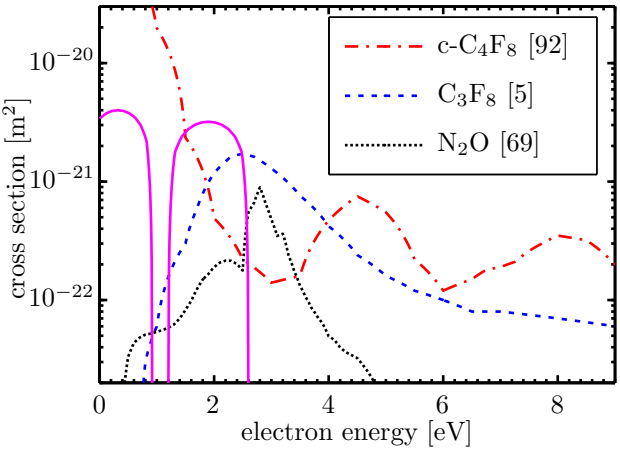

Figure 5.5.: Attachment cross sections of selected molecules reproduced from the literature, and preliminary ones of c-C_4F_8O (——).

the attachment cross sections require adjustment, when their energy dependence will be accurately known from future studies.

The electron attachment properties of c-C_4F_8O qualify this gas as useful additive to high voltage insulating gas mixtures. A delayed generation of electrons was presumed to occurr in N_2/c-C_4F_8O at high E/N with concurrent dissociation of c-C_4F_8O. These processes should be the subjects of future studies, given their impact on the performance of gaseous high voltage insulation.

6. Conclusions

Individual results of the present study have been discussed and provided with conclusions in previous chapters. In this chapter it is attempted to generalize the findings and to provide statements on gas mixtures of interest for high voltage insulation applications.

6.1. Progress of swarm methods

For historical and practical reasons, PT results have hitherto been expressed as spatial coefficients for ionization $[\alpha_{\mathrm{eff}}/N] = \mathrm{m}^2$ and diffusion $[ND_{\mathrm{L}}] = (\mathrm{sm})^{-1}$. These coefficients depend on the swarm drift velocity w. However, there is general agreement to interpret PT results by a temporal growth model [18, 19, 51].

To comply with a temporal model, the present PT results have been expressed as a rate constant $[\nu_{\mathrm{eff}}/N] = \mathrm{m}^3\mathrm{s}^{-1}$, and a gas density normalized diffusion time constant $[N\tau_{\mathrm{D}}] = \mathrm{sm}^{-3}$, respectively. These parameters are independent of w. A consistent set of swarm parameters can be obtained from PT measurements by mutually independent evaluation techniques, as we have demonstrated.

A lack of complete experimental swarm data was apparent for gas mixtures in the (E/N)-range near $(E/N)_{\mathrm{crit}}$. The presently adopted methods can provide accurate, high resolution data near $(E/N)_{\mathrm{crit}}$, which can improve the quantitative understanding of gaseous insulation.

An application of swarm methods to gas mixtures tends to produce extensive amounts of data. Thus, a linear response technique has been applied, which permits compact representation of swarm data for gas mixtures. The linear response data turned out to be

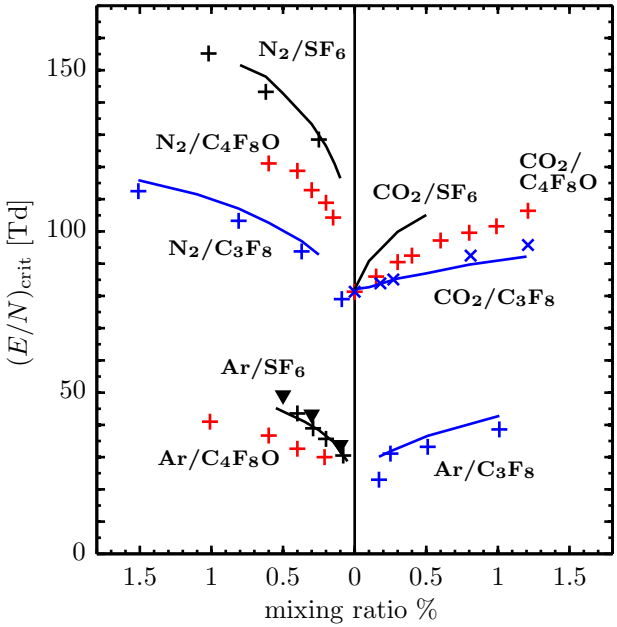

Figure 6.1.: Critical field strength of Ar, N_2 and CO_2 with small admixtures of attaching gases: (+, ×) experimental results, (——) calculated or simulated values [5, 18], and (▼) the calculations of Dincer [73]. Please note the *positive* values in both directions on the horizontal axis.

very useful for assessing electrical properties of gas mixtures. It was feasible to qualitatively describe previously unknown attachment cross sections of a molecule by comparing its linear responses with the corresponding data of more comprehensively known molecules. Moreover, the response data could be used in combination with numerical methods for estimating quantitative properties of the attachment cross sections of a molecule. Thus, the linear response technique consolidates the important role of swarm methods in studies of novel molecules.

6.2. Gas mixtures for high voltage insulation

The present results give examples of the determining influence of the electron energy distribution of the buffer gas on the rate constant of electron attachment to a gas additive. In order to achieve a high electrical strength of mixtures, it is necessary to identify gases with appropriate attachment cross sections to be added. Likewise, it is necessary to assess buffer gases for their usefulness in high voltage insulation [7].

Two criteria were provided for assessing the electrical strength of gas mixtures:

1. $(E/N)_{\mathrm{crit}}$ as a function of the mixing ratio.

2. The linear response as a function of E/N.

6.2.1. Comparison of N_2 and CO_2 buffer gases

We measured $(E/N)_{\mathrm{crit}} \approx 82$ Td for pure CO_2. In N_2, ν_{eff}/N was just detectable at 85 Td, but it was below the detection limit of SParX at 75 Td. Apparently, $(E/N)_{\mathrm{crit}}$ is very similar for N_2 and CO_2.

For the presently investigated gas additives, their mixtures with N_2 can provide higher $(E/N)_{\mathrm{crit}}$ than mixtures with CO_2, as one can see from figure 6.1. This is also the case for C_3F_8 mixtures,

even though the attachment rates to C_3F_8 are much higher in CO_2 than in N_2.

Clearly, the buffer gas plays a crucial role in the total energy loss of drifting electrons. A relative advantage of N_2 buffer gas over CO_2 can be deduced from the energy loss rate of drifting electrons, see e.g. definition (14) in [17].

6.2.2. Assessment of gas additives to N_2 and CO_2

SF_6 is a favourable additive [93]. The $(E/N)_{\mathrm{crit}}$-values of N_2/SF_6, see figure 6.1, can provide a benchmark for assessing other mixtures.

In the parameter range of the present study, N_2/c-C_4F_8O achieves about 85% of the benchmark at a given mixing ratio k. With respect to electron-molecule processes affecting the electron population, c-C_4F_8O is a useful additive to N_2, because the attachment cross sections overlap with densely populated intervals of the electron energy distribution in N_2.

The present thesis provides insight in the asymptotic behaviour of $(E/N)_{\mathrm{crit}}(k)$ with $k \to 0\%$. For N_2 or CO_2 buffer gases, any two $(E/N)_{\mathrm{crit}}$ curves originate at very similar ordinate values. In consequence, a ranking of gas additives can be based on measurements with $k \leq 1\%$ only, without the need to cover the entire range of k.

6.3. Outlook

In addition to the effects of electron-molecule collisions on the electron population, molecules can be involved with other processes in a buffer gas [93]. In the present study, dissociation of c-C_4F_8O and a delayed generation of electrons, with a cause other than electron-impact ionization, was observed for $(E/N) > (E/N)_{\mathrm{crit}}$ in N_2. Penning ionization and electron detachment are possible causes for a delayed generation of electrons [90, 91]. The effects of such processes can reduce the electrical strength of gaseous insulation, and they should be investigated in future studies.

Insulating gas mixtures should be carefully designed to mitigate the transfer of energy absorbed by the buffer gas to the additive, for example via dissociative quenching by metastables, via Penning ionization, or via photons. We have *not* found such processes to occurr with C_3F_8. Thus, it can be assumed that the Penning ionization rate is very small in N_2 mixtures when the ionization potential ε_i of the additive is ≥ 13.38 eV. It is a question of highly practical interest, if molecules with relatively low ε_i are per se disqualified as additives to N_2.

When the gas additive can produce O^-, it is important to consider chemical reactions of O^- in N_2 which lead to electron detachment [91]. It should be investigated if highly positive responses can possibly be found in N_2 with an additive predominantly forming O^-, or if molecules predominantly forming F^- are preferable. In N_2O/SF_6 for example, F^- is much more stable than O^- [94].

A. Tabulated experimental results

Pulsed Townsend measurements of the bulk velocity w, the effective ionization rate constant ν_{eff}/N, and the diffusion time constant $N\tau_{\text{D}}$ are given for selected values of the reduced electric field strength E/N which is in units of 1 Td $= 10^{-21}$ Vm^2.

Tables A.12 and A.13 give a list of linear response parameters r_{BA} for selected gas mixtures.

The precision of the data is:

- $\pm 1.5\%$ experimental uncertainty of E/N.
- $\pm 0.5\%$ statistical uncertainty[a)] of w.
- $\pm 2\%$ statistical uncertainty[a)] of $N\tau_{\text{D}}$.
- The statistical uncertainty[a)] of ν_{eff}/N is stated in the data tables, where it is larger than the rounding error.
- The statistical uncertainty[b)] of r_{BA} is stated in the data tables.

[a)] 99% confidence interval.
[b)] 95% confidence interval.

Table A.1.: Measured swarm parameters of Ar.

E/N (Td)	w (10^3 ms^{-1})	ν_{eff}/N (10^{-18} m^{3}s^{-1})	$N\tau_{\text{D}}$ (10^{16} sm^{-3})
11.0	10.6	$-0.03 \pm .01$	5.14
15.0	14.4	$-0.03 \pm .01$	3.13
19.0	18.0	$-0.02 \pm .01$	2.18
21.0	19.7	$0.02 \pm .01$	1.82
23.0	21.4	$0.08 \pm .01$	1.50
27.0	24.9	$0.29 \pm .01$	1.14
31.0	28.2	$0.71 \pm .01$	0.86
35.0	31.5	$1.36 \pm .02$	0.69
39.0	34.6	$2.34 \pm .03$	0.55
43.0	37.7	$3.59 \pm .05$	0.45
47.0	40.9	$5.14 \pm .06$	0.39
49.0	42.4	$5.76 \pm .07$	0.36

Table A.2.: 0.20% SF_6 in Ar.

E/N (Td)	w (10^3 ms^{-1})	ν_{eff}/N (10^{-18} m^{3}s^{-1})
19.0	17.9	$-1.47 \pm .01$
21.0	19.7	$-1.41 \pm .01$
23.0	22.0	$-1.38 \pm .01$
27.0	25.3	$-1.19 \pm .01$
31.0	28.2	$-0.76 \pm .01$
35.0	31.5	$-0.13 \pm .02$
37.0	33.0	$0.28 \pm .02$
41.0	36.1	$1.36 \pm .03$
45.0	39.9	$2.78 \pm .05$
47.0	41.4	$3.51 \pm .06$
49.0	43.1	$4.55 \pm .07$

Table A.3.: 0.51% C_3F_8 in Ar.

E/N (Td)	w (10^3 ms^{-1})	ν_{eff}/N (10^{-18} m^{3}s^{-1})
22.0	23.0	$-1.12 \pm .01$
26.0	25.5	$-0.90 \pm .01$
30.0	28.0	$-0.47 \pm .01$
34.0	30.9	$0.12 \pm .01$
38.0	33.8	$1.03 \pm .02$
42.0	37.3	$2.31 \pm .03$
46.0	40.8	$3.95 \pm .04$
50.0	43.8	$5.56 \pm .05$
54.0	47.0	$7.55 \pm .07$

Table A.4.: 0.21% c-C_4F_8O in Ar.

E/N (Td)	w (10^3 ms^{-1})	ν_{eff}/N (10^{-18} m^{3}s^{-1})	$N\tau_{\mathrm{D}}$ (10^{16} sm^{-3})
25	23.5	$-0.49 \pm .01$	1.13
27	25.6	$-0.34 \pm .01$	0.92
29	27.0	$-0.14 \pm .01$	0.82
31	28.8	$0.13 \pm .01$	0.74
33	30.4	$0.43 \pm .01$	0.67
35	31.7	$0.81 \pm .02$	0.61
37	33.4	$1.30 \pm .02$	0.54
39	35.1	$1.83 \pm .03$	0.50
41	36.8	$2.47 \pm .04$	0.46
43	38.4	$3.18 \pm .05$	0.42

Table A.5.: Measured swarm parameters of N_2.

E/N (Td)	w (10^3 ms^{-1})	ν_{eff}/N 10^{-18} m^{3}s^{-1}	$N\tau_{\text{D}}$ 10^{14} sm^{-3}
45.0	56.03	-0.04	6.09
55.0	65.11	-0.04	4.73
65.0	74.21	$-0.07 \pm .01$	4.50
75.0	83.58	$-0.06 \pm .01$	4.47
85.0	93.16	$0.10 \pm .01$	4.25
95.0	103.0	$0.53 \pm .01$	3.96
102.5	110.7	$1.09 \pm .01$	3.76
107.5	115.9	$1.60 \pm .02$	3.57
112.5	121.0	$2.44 \pm .02$	3.45
117.5	126.0	$3.29 \pm .04$	3.29
122.5	131.2	$4.60 \pm .04$	3.17
127.5	136.4	$5.84 \pm .07$	2.95
132.5	141.6	$7.85 \pm .07$	2.82
137.5	147.1	$10.52 \pm .13$	2.65
142.5	152.4	$13.25 \pm .12$	2.56
147.5	156.9	$16.48 \pm .17$	2.48
152.5	162.1	$19.99 \pm .18$	2.40
157.5	167.0	$22.66 \pm .12$	2.31
162.5	172.3	$27.09 \pm .14$	2.23
167.5	177.3	$29.72 \pm .16$	2.23
172.5	182.3	$34.96 \pm .21$	2.10
177.5	186.6	$38.34 \pm .22$	2.06

Table A.6.: 0.25% SF_6 in N_2.

E/N (Td)	w (10^3 ms^{-1})	ν_{eff}/N (10^{-18} m^{3}s^{-1})
65.0	73.9	$-13.6 \pm .1$
75.0	83.5	$-12.1 \pm .1$
85.0	93.7	$-10.8 \pm .1$
95.0	104	$-9.19 \pm .04$
105	114	$-7.42 \pm .03$
115	123	$-4.99 \pm .04$
125	134	$-1.61 \pm .07$
135	144	$2.92 \pm .10$
145	155	$9.22 \pm .15$
155	165	$17.3 \pm .2$
165	176	$25.4 \pm .3$

Table A.7.: 0.81% C_3F_8 in N_2.

E/N (Td)	w (10^3 ms^{-1})	ν_{eff}/N (10^{-18} m^{3}s^{-1})
20.0	31.8	$-0.61 \pm .01$
30.0	42.0	$-0.68 \pm .01$
40.0	51.6	$-0.75 \pm .01$
50.0	60.7	$-0.83 \pm .01$
60.0	69.6	$-0.92 \pm .01$
70.0	78.5	$-1.01 \pm .01$
80.0	87.6	$-1.05 \pm .01$
90.0	97.1	$-0.89 \pm .01$
100	107	$-0.36 \pm .01$
110	117	$0.76 \pm .02$
120	128	$2.72 \pm .05$
130	138	$5.75 \pm .08$
140	149	$10.4 \pm .2$
150	159	$16.7 \pm .2$

Table A.8.: 0.40% c-C_4F_8O in N_2.

E/N (Td)	w (10^3 ms^{-1})	ν_{eff}/N (10^{-18} m^{3}s^{-1})	$N\tau_{\mathrm{D}}$ (10^{15} sm^{-3})
22.5	33.8	$-2.64 \pm .02$	1.64
27.5	38.9	$-2.67 \pm .02$	1.22
32.5	43.9	$-2.76 \pm .02$	0.93
37.5	48.8	$-2.77 \pm .02$	0.74
45.0	55.8	$-2.78 \pm .02$	0.60
55.0	64.7	$-2.76 \pm .02$	0.48
65.0	73.6	$-2.67 \pm .02$	0.43
75.0	82.6	$-2.51 \pm .02$	0.41
85.0	92.0	$-2.21 \pm .01$	0.39
95.0	102	$-1.62 \pm .01$	0.38
105.0	113	$-0.59 \pm .01$	0.36
112.5	120	$0.55 \pm .02$	0.34
117.5	125	$1.62 \pm .03$	0.33
122.5	130	$2.97 \pm .05$	0.33
127.5	136	$4.59 \pm .07$	0.32

Table A.9.: Measured swarm parameters of CO_2.

E/N (Td)	w (10^3 m s^{-1})	ν_{eff}/N (10^{-18} m^3 s^{-1})	$N\tau_{\mathrm{D}}$ (10^{14} s m^{-3})
21.0	66.88	-0.09	13.1
23.0	74.32	-0.07	9.29
25.0	80.37	-0.09	7.16
27.0	84.96	-0.08	5.68
29.0	88.70	-0.07	4.93
32.0	93.12	-0.12	4.67
35.0	96.72	-0.15	4.79
38.0	99.65	-0.22	4.45
42.5	103.5	$-0.40 \pm .01$	4.29
47.5	107.1	$-0.65 \pm .01$	3.68
52.5	110.6	$-0.90 \pm .01$	3.58
57.5	114.1	$-1.14 \pm .01$	3.51
62.5	117.5	$-1.31 \pm .01$	3.51
67.5	120.9	$-1.34 \pm .01$	3.53
72.5	124.3	$-1.13 \pm .01$	3.52
77.5	127.8	$-0.65 \pm .02$	3.49
82.5	131.2	$0.17 \pm .03$	3.48
87.5	134.8	$1.36 \pm .04$	3.48
92.5	138.5	$2.92 \pm .06$	3.51
97.5	142.4	$5.00 \pm .07$	3.53
102.5	146.3	$7.37 \pm .10$	3.53
107.5	150.2	$10.17 \pm .14$	3.53
112.5	154.2	$14.03 \pm .20$	3.61
117.5	157.8	$18.74 \pm .29$	3.68
122.5	161.8	$23.47 \pm .32$	3.64

Table A.10.: 0.81% C_3F_8 in CO_2.

E/N (Td)	w (10^3 ms^{-1})	ν_{eff}/N (10^{-18} m^{3}s^{-1})
20.0	60.9	$-1.15 \pm .01$
28.0	85.1	$-2.24 \pm .03$
36.0	96.9	$-3.25 \pm .03$
44.0	104	$-3.99 \pm .02$
52.0	110	$-4.57 \pm .03$
60.0	116	$-4.99 \pm .03$
68.0	121	$-4.95 \pm .02$
76.0	127	$-4.32 \pm .02$
84.0	132	$-2.83 \pm .03$
92.0	137	$-0.21 \pm .02$
100	143	$3.56 \pm .07$
108	149	$8.75 \pm .11$
116	155	$15.8 \pm .2$

Table A.11.: 0.81% c-C_4F_8O in CO_2.

E/N (Td)	w (10^3 ms^{-1})	ν_{eff}/N (10^{-18} m^{3}s^{-1})	$N\tau_{\text{D}}$ (10^{14} sm^{-3})
22.5	70.1	$-8.6 \pm .1$	10.2
27.5	83.9	$-10.9 \pm .1$	5.88
35.0	94.8	$-11.6 \pm .1$	4.13
45.0	104	$-11.5 \pm .1$	3.31
55.0	112	$-11.2 \pm .1$	3.09
65.0	119	$-10.5 \pm .1$	3.05
75.0	126	$-9.1 \pm .1$	3.09
82.5	130	$-7.6 \pm .1$	3.13
87.5	134	$-5.9 \pm .1$	3.10
92.5	137	$-3.7 \pm .1$	3.08
97.5	141	$-1.2 \pm .1$	3.07
102.5	144	$1.7 \pm .1$	3.07
107.5	148	$5.4 \pm .1$	3.05
112.5	151	$9.6 \pm .1$	3.01

Table A.12.: Linear response r_{BA} of ν_{eff}/N on adding 1% C_3F_8 into N_2 or CO_2. The error corresponds to the 95% confidence interval of r_{BA}.

E/N (Td)	$r_{\mathrm{CO2/C3F8}}$ ($10^{-18}\mathrm{m^3s^{-1}}$)	E/N (Td)	$r_{\mathrm{N2/C3F8}}$ ($10^{-18}\mathrm{m^3s^{-1}}$)
28	$2.52 \pm .04$	20	$0.63 \pm .15$
32	$3.11 \pm .04$	30	$0.72 \pm .07$
36	$3.71 \pm .07$	40	$0.80 \pm .07$
44	$4.30 \pm .07$	50	$0.90 \pm .08$
52	$4.58 \pm .03$	60	$1.03 \pm .08$
60	$4.67 \pm .02$	70	$1.17 \pm .11$
68	$4.51 \pm .02$	80	$1.33 \pm .14$
76	$4.48 \pm .04$	90	$1.45 \pm .18$
84	$4.39 \pm .12$	100	$1.57 \pm .23$
92	$4.28 \pm .20$	110	$1.67 \pm .43$
100	$4.08 \pm .30$	120	$1.74 \pm .62$
108	$4.19 \pm .43$	130	$1.75 \pm .99$
116	$4.32 \pm .60$	140	$2.25 \pm .84$
		150	$2.09 \pm .51$

Table A.13.: Linear response r_{BA} of ν_{eff}/N on adding 1% c-C_4F_8O into N_2 or CO_2. The error corresponds to the 95% confidence interval of r_{BA}.

E/N (Td)	$r_{\mathrm{N2/c\text{-}C_4F_8O}}$ (10^{-18} $\mathrm{m^3s^{-1}}$)	$r_{\mathrm{CO2/c\text{-}C_4F_8O}}$ (10^{-18} $\mathrm{m^3s^{-1}}$)
22.5	12.2 ± 2.2	10.1 ± 1.1
25	12.0 ± 2.5	11.4 ± 1.2
30	12.2 ± 2.9	12.9 ± 1.1
36	12.7 ± 1.3	13.5 ± 1.5
42	12.8 ± 1.4	13.3 ± 1.5
48	12.7 ± 1.3	12.8 ± 1.4
56	12.6 ± 1.2	12.1 ± 1.2
64	12.4 ± 1.2	11.2 ± 1.2
72	12.0 ± 1.3	10.3 ± 1.0
82	11.3 ± 1.2	9.6 ± 0.8
92	10.6 ± 1.1	8.6 ± 0.8
102	9.6 ± 1.3	7.9 ± 1.2
112	9.2 ± 1.4	
122	8.6 ± 1.9	

Bibliography

[1] Roussel-Dupré R *et al* 2008 Physical processes related to discharges in planetary atmospheres *Space Sci. Rev.* **137** 51

[2] Christophorou L G and Olthoff J K 2002 Electron interactions with plasma processing gases: present status and future needs *Appl. Surface Sci.* **192** 309

[3] Kim K J *et al* 2004 Global warming gas emission during plasma cleaning process of silicon nitride using c-C_4F_8O/O_2 chemistry with additive Ar and N_2 *J. Vac. Sci. Tech. B* **22** 483

[4] Prager J, Riedel U and Warnatz J 2007 Modeling ion chemistry and charged species diffusion in lean methane-oxygen flames *Proc. Combustion Inst.* **31** 1129

[5] Biagi S F 1999 Monte Carlo simulation of electron drift and diffusion in counting gases under the influence of electric and magnetic fields *Nuclear Instr. and Meth. A* **421** 234

[6] Artuso M *et al* 2006 Performance of a C_4F_8O gas radiator ring imaging cherenkov detector using multi-anode photomultiplier tubes *Nuclear Instr. and Meth. A* **558** 373

[7] Christophorou L G 1988 Insulating gases *Nuclear Instr. and Meth. A* **268** 424

[8] Christophorou L G and Pinnaduwage L A 1990 Basic physics of gaseous dielectrics *IEEE Trans. El. Ins.* **25** 55

[9] Yousfi M, Robin-Jouan P and Kanzari Z 2005 Breakdown electric field calculations of hot SF_6 for high voltage circuit breaker applications *IEEE Trans. Diel. Ins.* **12** 1192

[10] Kumar K 1984 The physics of swarms and some basic questions of kinetic theory *Physics Reports* **112** 319

[11] Yamamoto O *et al* 2001 Applying a gas mixture containing c-C_4F_8 as an insulation medium *IEEE Trans. Diel. Ins.* **8** 1075

[12] Dujko S *et al* 2011 Boltzmann equation analysis of electron transport in a N_2-O_2 streamer discharge *Japanese J. Appl. Phys.* **50** DOI:10.1143/JJAP.50.08JC01

[13] Li C *et al* 2012 A comparison of 3D particle, fluid and hybrid simulations for negative streamers *Plasma Sources Sci. Tech.* **21** 55019

[14] Braun M, Marienfeld S, Ruf M-W and Hotop H 2009 High-resolution electron attachment to the molecules CCl_4 and SF_6 over extended energy ranges with the (EX)LPA method *J. Phys. B: At. Mol. Opt. Phys.* **42** 125202

[15] Khakoo M A, Zatsarinny O and Bartschat K 2011 Near-threshold electron impact excitation of the argon $3p^5 4s$ configuration - new and revised normalized differential cross sections using recent time-of-flight measurements for normalization *J. Phys. B: At. Mol. Opt. Phys.* **44** 15201

[16] Buckman S J and Brunger M J 1997 A critical comparison of electron scattering cross sections measured by single collision and swarm techniques *Aust. J. Phys.* **50** 483

[17] Robson R E, White R D and Petrović Z L 2005 Physically based fluid modeling of collisionally dominated low-temperature plasmas *Rev. Mod. Phys.* **77** 1303

[18] Hagelaar G J M and Pitchford L C 2005 Solving the Boltzmann equation to obtain electron transport coefficients and rate coefficients for fluid models *Plasma Sources Sci. Tech.* **14** 722

[19] Tagashira H, Sakai Y and Sakamoto S 1977 The development of electron avalanches in argon at high E/N values. II. Boltzmann equation analysis *J. Phys. D: Appl. Phys.* **10** 1051

[20] Petrović Z L *et al* 2009 Measurement and interpretation of swarm parameters and their application in plasma modelling *J. Phys. D: Appl. Phys.* **42** 194002

[21] Raether H *Electron Avalanches and Breakdown in Gases* Butterworth (London) 1964

[22] Franck C M *et al* 2013 An efficient procedure to identify and quantify new molecules for insulating gas mixtures *Contrib. Plasma Phys.* **53** DOI:10.1002/ctpp.201300030

[23] Jiang X, Berglund C N, Bell A E, Mackie W A 1998 Photoemission from gold thin films for application in multiphotocathode arrays for electron beam lithography *J. Vac. Sci. Tech. B* **16** 3374

[24] Janzen A *et al* 2007 A pulsed electron gun for ultrafast electron diffraction at surfaces *Rev. Sci. Instr.* **78** 13906

[25] Karrer R *et al* 2001 Design of a miniature picosecond low-energy electron gun for time-resolved scattering experiments *Rev. Sci. Instr.* **72** 4404

[26] Wang Y, Christophorou L G and Verbrugge J K 1998 Effect of temperature on electron attachment to and negative ion states of CCl_2F_2 *J. Chem. Phys.* **109** 8304

[27] Kopyra J, Wnorowska J, Foryś M and Szamrej I 2007 A new apparatus for measuring rate constants and activation energies

of thermal electron capture processes in the gas phase *Int. J. Mass Spectr.* **268** 60

[28] de Urquijo J, Arriaga C A, Cisneros C and Alvarez I 1999 A time-resolved study of ionization, electron attachment and positive-ion drift in methane *J. Phys. D: Appl. Phys.* **32** 41

[29] Verhaart H F A and van der Laan P C T 1982 Fast current measurements for avalanche studies *J. Appl. Phys.* **53** 1430

[30] Breskin A 1996 CsI UV photocathodes: history and mystery *Nuclear Instr. and Meth. A* **371** 116

[31] Wrobel R J and Becker S 2010 Carbon and sulphur on Pd(111) and Pt(111): Experimental problems during cleaning the substrates and impact of sulphur on the redox properties of CeO_x in the CeO_x/Pd(111) system *Vacuum* **84** 1258

[32] Fowler R H 1931 The analysis of photoelectric sensitivity curves for clean metals at various temperatures *Phys. Rev.* **38** 45

[33] Moruzzi J L 1967 High emission photocathode for swarm experiments *Rev. Sci. Instr.* **38** 1284

[34] Dannetun H M, Lundström I and Petersson L-G 1988 Reactions between hydrocarbons and an oxygen covered palladium surface *Surface Sci* **193** 109

[35] Aschwanden T Ph.D. dissertation ETH Zurich 1985 Diss. ETH Nr. 7931

[36] Price D A, Lucas J and Moruzzi J L 1972 Ionization in oxygen-hydrogen mixtures *J. Phys. D: Appl. Phys.* **5** 1249

[37] Yamaji M, Nakamura Y and Morokuma Y 2004 Measurements of ionization and attachment coefficients in 0.468% and 4.910% c-C_4F_8/Ar mixtures and pure c-C_4F_8 *J. Phys. D: Appl. Phys.* **37** 432

[38] Stelman D, Moruzzi J L and Phelps A V 1972 Low energy electron attachment to ozone using swarm techniques *J. Chem. Phys.* **56** 4183

[39] Lakdawala V K and Moruzzi J L 1980 Measurements of attachment coefficients in NF_3-nitrogen and NF_3-rare gas mixtures using swarm techniques *J. Phys. D: Appl. Phys.* **13** 377

[40] Petersson L-G, Dannetun H M and Lundström I 1985 The water-forming reaction on palladium *Surface Sci* **161** 77

[41] Dahl D A, Teich T H and Franck C M 2012 Obtaining precise swarm parameters from a pulsed Townsend setup *J. Phys. D: Appl. Phys.* **45** 485201

[42] Wetzer J M, Wen C and van der Laan P C T 1988 Bandwidth limitations of gap current measurements *Conf. Record of the 1988 IEEE Int. Symposium on Electrical Insulation* **1** 355

[43] Fletcher J 1985 Non-equilibrium in low pressure rare gas discharges *Aust. J. Phys.* **18** 221

[44] Dujko S, White R D and Petrović Z L 2008 Monte Carlo studies of non-conservative electron transport in the steady-state Townsend experiment *J. Phys. D: Appl. Phys.* **41** 245205

[45] White R D, Robson R E, Nicoletopoulos P and Dujko S 2012 Periodic structures in the Franck-Hertz experiment with neon: Boltzmann equation and Monte-Carlo analysis *Eur. Phys. J. D* **66** 117

[46] Blevin H A and Fletcher J 1992 Optical studies of pre-breakdown electron avalanches *Aust. J. Phys.* **45** 375

[47] Napartovich A P and Kochetov I V 2011 The value of swarm data for practical modeling of plasma devices *Plasma Sources Sci. Tech.* **20** 25001

[48] Samukawa S *et al* 2012 The 2012 plasma roadmap *J. Phys. D: Appl. Phys.* **45** 253001

[49] Montijn C and Ebert U 2006 Diffusion correction to the Raether-Meek criterion for the avalanche-to-streamer transition *J. Phys. D: Appl. Phys.* **39** 2979

[50] Suvakov M *et al* 2005 Spatial profiles of electron swarms properties and explanation of negative mobility of electrons *IEEE Trans. Plasma Sci.* **33** 532

[51] Dujko S, White R D, Raspopović Z M and Petrović Z L 2012 Spatially resolved transport data for electrons in gases: Definition, interpretation and calculation *Nuclear Instr. and Meth. B* **279** 84

[52] Hernández-Ávila J L, Basurto E and de Urquijo J 2002 Electron transport and swarm parameters in CO_2 and its mixtures with SF_6 *J. Phys. D: Appl. Phys.* **35** 2264

[53] Ridenti M A, Vivaldini T C, Lima I B and Pascholati P R 2010 A method for evaluating electron transport parameters on a pulsed Townsend experiment *AIP Conf. Proc.* **1245** 92

[54] Ramo S 1939 Currents induced by electron motion *Proc. I.R.E.* **27** 584

[55] Nakamura Y and Kuraichi M 1987 Drift velocity and longitudinal diffusion coefficient of electrons in nitrogen and carbon monoxide *J. Phys. D: Appl. Phys.* **20** 933

[56] Townsend J S and MacCallum S P 1929 Ionization by collision in monatomic gases *Proc. of the Royal Society London* **124** 533

[57] Nakamura Y and Kuraichi M 1988 Electron transport parameters in argon and its momentum transfer cross section *J. Phys. D: Appl. Phys.* **21** 718

[58] Elford M T and Haddad G N 1980 The drift velocity of electrons in carbon dioxide at temperatures between 193 and 573 K *Aust. J. Phys.* **33** 517

[59] Haydon S C and Williams O M 1976 Combined spatial and temporal studies of ionization growth in nitrogen *J. Phys. D: Appl. Phys.* **9** 523

[60] Bhalla M S and Craggs J D 1976 Measurement of ionization and attachment coefficients in carbon dioxide in uniform fields *Proc. Phys. Soc.* **76** 369

[61] Brunger M J and Buckman S J 2002 Electron-molecule scattering cross-sections. I. Experimental techniques and data for diatomic molecules *Physics Reports* **357** 215

[62] Anzai K *et al* 2012 Cross section data sets for electron collisions with H_2, O_2, CO, CO_2, N_2O and H_2O *Eur. Phys. J. D* **66** 36

[63] Itikawa Y 2006 Cross sections for electron collisions with nitrogen molecules *J. Phys. Chem. Ref. Data* **35** 31

[64] Hernández-Ávila J L, Basurto E and de Urquijo J 2004 Electron transport and ionization in CHF_3−Ar and CHF_3−N_2 gas mixtures *J. Phys. D: Appl. Phys.* **37** 3088

[65] Raju G G *Gaseous Electronics - Tables, Atoms, and Molecules* CRC Press (Boca Raton, CA) 2012

[66] Dahl D A and Franck C M 2013 Response analysis of electron attachment rates to C_3F_8 and SF_6 in buffer gases *J. Phys. D: Appl. Phys.* **46** 445202

[67] Hunter S R and Christophorou L G 1984 Electron attachment to perfluoroalkanes n-C_NF_{2N+2} $N = 1 - 6$ using high pressure swarm techniques *J. Chem. Phys.* **80** 6150

[68] Rosa A, Barszczewska W, Foryś M and Szamrej I 2001 Electron capture by haloethanes in a carbon dioxide buffer gas *Int. J. Mass Spectr.* **205** 85

[69] Dupljanin S *et al* 2010 Transport coefficients and cross sections for electrons in N_2O and N_2O/N_2 mixtures *Plasma Sources Sci. Tech.* **19** 25005

[70] Bordage M C, Ségur P and Chouki A 1996 Determination of a set of electron impact cross sections in tetrafluoromethane consistent with experimental determination of swarm parameters *J. Appl. Phys.* **80** 1325

[71] Hunter S R, Carter J G and Christophorou L G 1989 Low energy electron attachment to SF_6 in N_2, Ar, and Xe buffer gases *J. Chem. Phys.* **90** 4879

[72] Dincer M S, Ozerdem O C and Bektas S 2007 Effective ionization coefficients and transport parameters in ultradilute SF_6+N_2 mixtures *IEEE Trans. Plasma Sci.* **35** 1210

[73] Cekmen Z C and Dincer M S 2009 Effective ionization coefficients and transport parameters in binary and ultradilute SF_6-Ar mixtures using Boltzmann equation analysis *J. Phys. D: Appl. Phys.* **42** 145208

[74] Christophorou L G and Olthoff J K 2000 Electron interactions with SF_6 *J. Phys. Chem. Ref. Data* **29** 267

[75] Christophorou L G and Olthoff J K 1998 Electron interactions with C_3F_8 *J. Phys. Chem. Ref. Data* **27** 889

[76] Christophorou L G and Olthoff J K 1999 Electron interactions with plasma processing gases: An update for CF_4, CHF_3, C_2F_6 and C_3F_8 *J. Phys. Chem. Ref. Data* **28** 967

[77] Jeon B-H 2006 Determination of electron collision cross-sections for the C_3F_8 molecule by using an electron swarm study *Journal of the Korean Physical Society* **49** 2321

[78] Baio J E *et al* 2007 Electron-impact dissociation cross sections for CHF_3 and C_3F_8 *J. Phys. D: Appl. Phys.* **40** 6969

[79] Spyrou S M and Christophorou L G 1985 Effect of temperature on the dissociative and nondissociative electron attachment to C_3F_8 *J. Chem. Phys.* **83** 2829

[80] Blevin H A, Fletcher J and Hunter S R 1985 Electron-velocity distribution functions in gases: The influence of anisotropic scattering and electron nonconservation by attachment and ionization *Phys. Rev. A* **31** 2215

[81] Dyatko N A *et al* 2000 On the possibility of negative electron mobility in a decaying plasma *J. Phys. D: Appl. Phys.* **33** 375

[82] Dyatko N A and Napartovich A P 1999 Electron swarm characteristics in Ar:NF_3 mixtures under steady-state Townsend conditions *J. Phys. D: Appl. Phys.* **32** 3169

[83] Itoh H *et al* 1993 Electron transport coefficients in SF_6 *J. Phys. D: Appl. Phys.* **26** 1975

[84] Pancheshnyi *et al* 2012 The LXCat project: Electron scattering cross sections and swarm parameters for low temperature plasma modeling *Chem. Phys.* **398** 148

[85] Phelps A V and van Brunt R J 1988 Electron transport, ionization, attachment, and dissociation coefficients in SF_6 and its mixtures *J. Appl. Phys.* **64** 4269

[86] Warren K J, Tuma P E, Owens J G and Minday R M 2011 Perfluoroketones as gaseous dielectrics *PCT* WO2011/090992

[87] Ingold M *et al* 2012 Dielectric insulation medium *WIPO* WO2012/080269

[88] Piccoz D, Kieffel Y and Girodet A 2012 Method for fillig gas-insulated electrical equipment *WIPO* WO2013/045397

[89] Rabie M *et al* 2013 Predictors for gases with high electrical strength *IEEE Trans. Diel. Ins.* **20** 856

[90] Bekstein A, de Urquijo J, Hernández-Ávila J L and Basurto E 2012 Measurement of electron swarm coefficients in C_2F_4−Xe and evidence of Penning ionization in C_2F_4−Ar *Eur. Phys. J. D* **66** 77

[91] Frommhold L 1964 Über verzögerte Elektronen in Elektronenlawinen, insbesondere in Sauerstoff und Luft, durch Bildung und Zerfall negativer Ionen (O^-) *Fortschritte der Physik* **12** 597

[92] Christophorou L G and Olthoff J K 2001 Electron interactions with c-C_4F_8 *J. Phys. Chem. Ref. Data* **30** 449

[93] Christophorou L G and van Brunt R J 1995 SF_6/N_2 mixtures basic and HV properties *IEEE Trans. Diel. Ins.* **2** 952

[94] Basurto E, Hernández-Ávila J L, Juárez A M and de Urquijo J 2013 Electron swarm coefficients and limiting field strength of SF_6−N_2O mixtures *J. Phys. D: Appl. Phys.* **46** 355207

List of publications

1. Dahl D A and Franck C M 2010 **conference paper** Pulsed Townsend technique in electronegative gases *International Conference on Gas Discharges and Their Applications* Greifswald (Germany).

2. Dahl D A and Franck C M 2011 **presentation** Sampling the low-energy range of EEDF *Gaseous Electronics Conference* Salt Lake City (Utah, USA).

3. Dahl D A and Franck C M 2012 **presentation** Elektronenschwärme in elektronegativen Gasmischungen *DPG Frühjahrstagung, section plasma physics* Stuttgart (Germany).

4. Dahl D A, Teich T H and Franck C M 2012 **journal paper** Obtaining precise electron swarm parameters from a pulsed Townsend setup *Journal of Physics D: Applied Physics* **45** 485201.

5. Dahl D A and Franck C M 2013 **poster contribution** Attachment cross sections of c-C_4F_8O estimated from swarm measurements in Ar, N_2 or CO_2 *DPG Frühjahrstagung, section plasma physics* Jena (Germany). Awarded with poster prize.

6. Rabie M, Dahl D A, Donald S M A, Reiher M and Franck C M 2013 **journal paper** Predictors for Gases of High Electrical Strength *IEEE Transactions on Dielectrics and Electrical Insulation* **20** 856.

7. Dahl D A and Franck C M 2013 **journal paper** Response analysis of electron attachment rates to C_3F_8 and SF_6 in buffer gases *Journal of Physics D: Applied Physics* **46** 445202.

8. Franck C M, Dahl D A, Rabie M, Häfliger P and Koch M 2013 **journal paper** An efficient procedure to identify and quantify new molecules for insulating gas mixtures *Contributions to Plasma Physics* **53** DOI:10.1002/ctpp.201300030.

9. Dahl D A and Franck C M 2013 **submitted** Electron attachment to c-C_4F_8O from swarm measurements in a buffer gas of Ar, N_2 or CO_2 *European Physical Journal D, POSMOL special issue.*

Acknowledgements

The project at hand was initiated and set on the right track by Professor C.M. Franck. I am especially grateful to him for having allowed me a free hand in project implementation, and an undisturbed period of thesis writing.

With all my heart I thank the administrative, technical and scientific colleagues of our institute for the very effective cooperation and the very pleasant time spent together. Mechanical, electronical, and mechatronical services were skillfully provided by H. Kienast and D. Brühlmann during the experimental implementations. I have much appreciated collaborating with them. Many highly motivated students have successfully contributed their work to the present research project: L. Zurbuchen, M. Darbellay, M. Läubli, V. Keryulis, and P. Häfliger.

To A. Bitschi, I am profoundly grateful for his preparing the technical drawings and production orders of the photocathode mount. The service of H.R. Scherrer and S. Tigermann is gratefully acknowledged as they have coated the photocathode substrates. I am much indebted to S.F. Biagi and H.J. Teunissen who provided their simulation results and thus stimulated an important progress of my work.

I want to express my very sincere thanks to T.H. Teich for teaching me how to forge lab work into scientific articles. Max has been very pleased about a continuous supply of shortbread.

My family must be praised for their continuous efforts in giving me support. Maybe my presence at home was not always enough but sufficient.